OPEN ACCESS
IOP Publishing
Plasma Sources Science and Technology
Plasma Sources Sci. Technol. **33** (2024) 055003 (20pp)
https://doi.org/10.1088/1361-6595/ad4055

Surface recombination in Pyrex in oxygen DC glow discharges: mesoscopic modelling and comparison with experiments

Pedro Viegas[1,*], **Jorge Silveira**[1], **Tiago Cunha Dias**[1], **Olivier Guaitella**[2], **Ana Sofía Morillo Candás**[2] and **Vasco Guerra**[1]

[1] Instituto de Plasmas e Fusão Nuclear, Instituto Superior Técnico—Universidade de Lisboa, Av. Rovisco Pais 1, 1049-001 Lisboa, Portugal
[2] Laboratoire de Physique des Plasmas (UMR 7648), CNRS, Univ. Paris-Saclay, Sorbonne Université, École Polytechnique, Palaiseau, France

E-mail: pedro.a.viegas@tecnico.ulisboa.pt

Received 16 February 2024, revised 3 April 2024
Accepted for publication 18 April 2024
Published 7 May 2024

Abstract

Surface recombination in an oxygen DC glow discharge in a Pyrex (borosilicate glass) tube is studied via mesoscopic modelling and comparison with measurements of recombination probability. A total of 106 experimental conditions are assessed, with discharge current varying between 10 and 40 mA, pressure values ranging between 0.75 and 10 Torr, and fixed outer wall temperatures (T_w) of −20, 5, 25 and 50 °C. The model includes O+O and O+O_2 surface recombination reactions and a T_w dependent desorption frequency. The model is validated for all the 106 studied conditions and intends to have predictive capabilities. The analysis of the simulation results highlights that for $T_w = -20\,°C$ and $T_w = 5\,°C$ the dominant recombination mechanisms involve physisorbed oxygen atoms (O_F) in Langmuir–Hinshelwood (L-H) recombination $O_F + O_F$ and in Eley–Rideal (E-R) recombination $O_2 + O_F$, while for $T_w = 25\,°C$ and $T_w = 50\,°C$ processes involving chemisorbed oxygen atoms (O_S) in E-R $O + O_S$ and L-H $O_F + O_S$ also play a relevant role. A discussion is taken on the relevant recombination mechanisms and on ozone wall production, with relevance for higher pressure regimes.

Supplementary material for this article is available online

Keywords: oxygen kinetics, surface kinetics, oxygen loss probability, ozone production, oxygen recombination

---

[*] Author to whom any correspondence should be addressed.

1. Introduction

The interaction between low-temperature plasmas and surfaces is of paramount importance in various scientific and technological domains. Understanding it is crucial to advance materials science, biomedicine and nanotechnology, potentially helping to optimize plasma-based processes such as plasma etching, surface modification, thin film deposition, plasma-tissue treatment and atmospheric entry. In essence, delving into the interdisciplinary field of plasma-surface interactions not only enhances our fundamental understanding of the interdependence between two media in direct contact but also paves the way for ground-breaking technological innovations with far-reaching implications.

Low-temperature plasmas are known to modify solid surfaces by providing charges and reactive and energetic gaseous species (Oehrlein 1997, Kersten *et al* 2001, Vanraes *et al* 2021). However, the densities of active gaseous species in the plasma are also affected by surface kinetics. As such, a detailed understanding of this kinetics is often required to control plasma properties and design plasma processes (Kushner 2009, Murphy and Park 2017, Bogaerts *et al* 2022). Indeed, self-consistent macroscopic models, either fluid or kinetic, require an accurate description of the interaction of the plasma with the surface. However, the surface interaction data strongly depend on working conditions and are often derived from fitting experimental measurements obtained for a particular condition, which limits the predictive capabilities of models dependent on plasma-surface interactions.

Oxygen plasmas are widely used in material processing applications and in biomedical applications at high pressure. In particular, atomic oxygen is a key reactive species for many plasma processing applications. It is also a main species of interest for product separation in plasmas for electrochemical conversion at intermediate and high pressures (Rohnke *et al* 2004, Chen *et al* 2020, Pandiyan *et al* 2022). The main mechanism of production of O atoms in pure oxygen plasmas is electron impact dissociation of O_2. At pressures below tens of Torr, three-body collisions in the plasma volume have low probability and thus O atoms are predominantly lost by surface recombination back into O_2 (Gousset *et al* 1987, Macko *et al* 2004, Annušová *et al* 2018, Dias *et al* 2023). The probability for this latter process, γ_O, defined as the ratio between the number of atoms that successfully recombine on the surface and all the atoms that strike the wall, is highly dependent on the type of surface and on working conditions of pressure, current, gas temperature and wall temperature. Hence, atomic oxygen surface recombination is a very complex process and has been widely studied in plasma reactors for different conditions and surfaces. These studies are listed and compared in the recent review by Paul *et al* (2023). The recombination is very effective (above 10%) on metallic and catalytic surfaces (Morgan and Schiff 1964, Mozetic and Cvelbar 2007, Mozetic *et al* 2015), less effective on crystals and semi-catalytic surfaces and even less (below 1%) on inert materials like silica-based or glass-based materials such as Pyrex and quartz. These materials are common in plasma reactors and several studies have measured the dependence of O recombination on surface temperature and other parameters for Pyrex (Pagnon *et al* 1995, Macko *et al* 2004, Booth *et al* 2019, 2020), for quartz (Kim and Boudart 1991, Balat-Pichelin *et al* 2003, Cartry *et al* 2006, Lopaev *et al* 2011a) and similar materials (Rakhimova *et al* 2009, Krištof *et al* 2012). Moreover, atomic oxygen recombination in silica-like materials is of paramount importance in defining the heat transfer to the surface of space vehicles in atmospheric re-entry conditions (Kovalev *et al* 2005, Kovalev and Kolesnikov 2005, Bourdon and Bultel 2008).

The same recombination process can be studied theoretically and numerically (Cacciatore *et al* 1999, Rutigliano and Cacciatore 2016). Plasma-surface interactions take place in multiple time scales. The shortest time-scale, of the order of fs, is associated with the vibrational motion of adsorbed species (Graves and Brault 2009, Neyts and Brault 2017). The description of elementary steps of adsorption, desorption, diffusion, and reactions on the surface on the atomic level occurs in time-scales in the range ns-ms (Guerra and Marinov 2016). However, experiments often involve an evolving surface dynamics during several minutes. Mesoscopic models are a solution to bridge the gap between the detailed atomistic description and the macroscopic scales of real systems (Alves *et al* 2018). These are coarse-grained models describing surfaces and their occupation by surface site densities and surface species densities. In these models, the system evolution is described by a series of reactions with prescribed rates. Mesoscopic models can adopt a stochastic (Guerra and Loureiro 2004, Guerra and Marinov 2016, Marinov *et al* 2017) or a deterministic description of the system, whose mathematical resolution can be either analytical (Guerra 2007, Rakhimova *et al* 2009, Lopaev *et al* 2011a, Booth *et al* 2019) or numerical (Gordiets *et al* 1996, Gordiets and Ferreira 1998, Cartry *et al* 2000). They require as input the energy barriers for each elementary step and other physical parameters that depend on the atomistic interactions described by more microscopic models, and thus are not fully self-consistent. However, mesoscopic models can effectively provide an interesting physical insight of the surface kinetics processes, receiving input from the gas phase chemistry and be used to describe both the steady-state and the dynamics of the system up to any time-scale.

Despite the wide variety of models and experimental conditions, there is a widely accepted view of atom surface recombination processes (Seward and Jumper 1991, Cacciatore and Rutigliano 2009). It can generally occur via two mechanisms: Eley–Rideal (E-R) processes where a particle from the gas phase directly recombines with an adsorbed (chemisorbed or physisorbed) particle, which are thus dependent on the adsorbed density to the first order; Langmuir–Hinshelwood (L-H) processes where a physisorbed particle diffuses along the surface and recombines with another adsorbed particle, that are dependent on the adsorbed density to the second order. In the case of oxygen plasmas, if E-R and L-H processes involve one oxygen atom O and one oxygen molecule O_2, they can give origin to ozone O_3, another interesting species for applications such as air and water treatment. These surface processes were evidenced on silica-like materials by experiments by Janssen and Tuzson (2010) and by Marinov *et al* (2013a) and studied numerically by Lopaev *et al* (2011a, 2011b), by Marinov *et al* (2013b) and by Guerra *et al* (2019). More recently, the ozone kinetics, including its surface production, was investigated by Booth *et al* (2023) and by Meyer *et al* (2023) on Pyrex (borosilicate glass). Concerning O atom recombination as a whole, several experimental and modelling works have assessed the relative importance and the characteristic parameters of E-R and L-H mechanisms in oxygen plasmas, as this evaluation can change the predictive accuracy of mesoscopic models (Macko *et al* 2004, Guerra 2007, Guerra and Marinov 2016, Booth *et al* 2019, Guerra *et al* 2019).

Booth *et al* (2019) recently studied the recombination of O atoms on the surface of a Pyrex (borosilicate glass, $SiO_2 + B_2O_3$) tube containing a pure O_2 DC glow discharge over the pressure range 0.2–10 Torr and the current range 10–40 mA, for fixed outer wall temperatures of 5 °C and 50 °C. The atom loss rate was measured through optical emission actinometry with current modulation and the atom recombination probability γ_O was deduced from it. The value of γ_O passes through a minimum at approximately 0.75 Torr. At pressures below this minimum, γ_O decreases with pressure and increases strongly with the discharge current. This effect was attributed by Booth *et al* (2019) to incident ions and fast neutrals with sufficient kinetic energy to clean or chemically modify the surface, generating new adsorption sites. This idea was further developed by Afonso *et al* (2024). At pressures above 0.75 Torr, Booth *et al* (2019) found an approximate Arrhenius behaviour of γ_O with the incident atom temperature. γ_O falls below the Arrhenius law when the temperature and the O flux are lower. The authors explained these results by an E-R mechanism with incident O atoms recombining with both chemisorbed and more weakly bonded physisorbed atoms on the surface. Booth *et al* (2019) proposed a phenomenological E-R model that explains the observed behaviour while depending only on a minimum set of parameters that are adjusted to match a large set of experimental measurements.

Despite considering a low desorption frequency and highlighting the role of physisorbed atoms in O recombination, Booth *et al* (2019) neglect L-H mechanisms, as well as the impact of O_2 and of O_3 production on the surface. Indeed, the model by Booth *et al* (2019) may correspond to an effective way of capturing to some extent a more complex physical picture. However, a more accurate description of O atom surface recombination on Pyrex may be required to clarify the dominant mechanisms. Such a description should result in modelling with predictive capabilities, being able to foresee the influence of plasma-surface interactions in different systems where these play an important role. The works in the PhD thesis by Morillo-Candás (2019) and in the MSc thesis by Silveira (2023) employed a mesoscopic model to assess the influence of different surface mechanisms (those suggested by Booth *et al* (2019) and others) on O atom recombination in the same conditions studied by Booth *et al* (2019). Parametric studies were done to feed the investigation of the importance of different mechanisms. This work builds on those studies to develop a more complete description of surface kinetics of O atom recombination in Pyrex in oxygen discharges. Despite the large number of studies of O recombination on Pyrex, the results are rather inconsistent, showing a large irreproducibility attributed to different experimental conditions (e.g. different recombination probabilities are found by Booth *et al* (2019) and Booth *et al* (2020)). As such, a model validated against consistent and reproducible measurements is still lacking, that can provide a complete description and evaluation of recombination mechanisms in a widely used material in plasma reactors such as Pyrex.

In this work, mesoscopic modelling of surface processes is employed to assess the interaction between an oxygen DC glow discharge and a Pyrex surface in the conditions studied by Booth *et al* (2019) and in additional conditions. The experimental conditions are presented in section 2. Two experimental data sets are taken and described. One from Booth *et al* (2019) at wall temperatures of 5 °C and 50 °C. Another one from the MSc thesis by Dias (2019) in similar conditions at wall temperatures of −20 °C, 5 °C, 25 °C and 50 °C. The mesoscopic surface kinetics model used in this work is described in section 3, together with three different reaction sets. The simplest one is the set by Booth *et al* (2019), effective at describing experimental results with a minimum set of parameters but neglecting likely relevant processes. Then, the base reaction set employed in previous works (Guerra and Marinov 2016, Marinov *et al* 2017) is recalled and further developed into an upgraded reaction set providing a more complete description of surface kinetics while keeping the simplicity of a mesoscopic model. The upgraded model considers the kinetics of impacting O_2 and of O_3 surface production and assumes a desorption frequency dependent on wall temperature. The results of the upgraded model are validated against the two sets of experimental data in section 4.1 and the relevance of different recombination mechanisms is analysed in section 4.2. These are further discussed, together with the surface mechanisms for ozone production, via literature comparisons, in section 4.3. Finally, the conclusions are summarized in section 5.

2. Discharge set-up and conditions

The discharge conditions studied experimentally and numerically by Booth *et al* (2019, 2020, 2022, 2023), Western *et al* (2020), Viegas *et al* (2023)and Dias *et al* (2023) are assessed in this work. The experimental set-up is described in detail by Booth *et al* (2019, 2020, 2022, 2023)and a simplified scheme is presented in figure 1, adapted from the work by Booth *et al* (2019). It consists of a DC glow discharge in O_2, ignited in a Pyrex (borosilicate glass) tube of 2 mm thickness, 1.0 cm inner radius and 56 cm length. The discharge is ignited by electrodes located in side-arms separated by 52.5 cm. The discharge current is varied between 10 mA and 40 mA and the pressure values are changed within the interval between 0.2 Torr (0.27 mbar) and 10 Torr (13.33 mbar). In this work, only the high pressure regime identified by Booth *et al* (2019) for pressures of 0.75 Torr (1 mbar) and above is addressed. In these conditions, ions are assumed to have low energies and

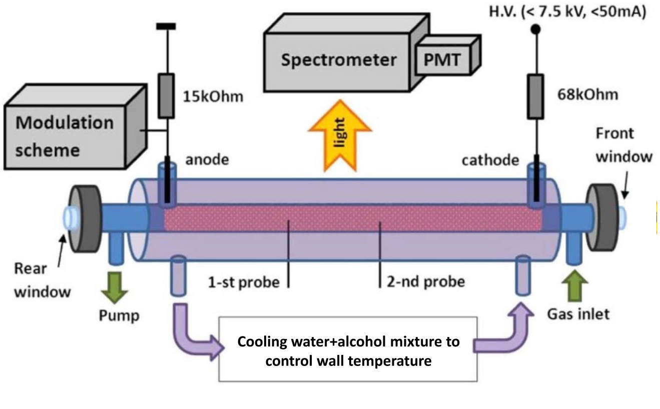

Figure 1. Scheme of the experimental set-up. Adapted from Booth *et al* (2019). © IOP Publishing Ltd. All rights reserved.

thus to not modify the surface. The surface kinetics of atomic oxygen recombination in Pyrex for pressures below 0.75 Torr, conditions in which the ion kinetic energy can have an effect on surfaces, was recently addressed by Booth *et al* (2019) and by Afonso *et al* (2024). The cylindrical tube outer surface is kept at a constant temperature variable between −20 °C and 50 °C. This is guaranteed by a water/ethanol mixture flowing through an outer envelope and connected to a thermostatic bath. The temperature drop across the Pyrex tube wall is considered to be negligible, of less than 2 K (Booth *et al* 2019). The gas flow rate is kept low, between 3 sccm and 10 sccm, as to ensure that the gas residence time (>1 s) is longer than the lifetime of all the active species in the discharge. The leak rate of air into the system is small, below 0.015 sccm, corresponding in the worst case to less than 0.4% N_2 in the mixture. Such a N_2 concentration in O_2 gas is not expected to have any noticeable effect neither on discharge parameters nor on the kinetics of oxygen plasma species. As a result, an axially uniform plasma column is studied with constant gas composition (almost pure O_2) and cylindrical symmetry, in interaction with the cylindrical Pyrex vessel. Two experimental data sets are addressed in this work, which provide the input conditions for the surface models and the experimental outputs to compare with simulations and study surface recombination.

2.1. Experimental data from Booth et al (2019): data set 1

Data set 1 was obtained by Booth *et al* (2019) and shared by the authors. It contains a total of 56 different conditions: 28 for wall temperature $T_\mathrm{w} = 5\,^\circ\mathrm{C}$ and 28 for $T_\mathrm{w} = 50\,^\circ\mathrm{C}$. These include pressure values of 0.75, 1, 1.5, 2, 3, 5, 7.5 and 10 Torr and currents of 10, 20, 30, and 40 mA. For each condition, the gas temperature was measured from the rotational structure of the $O_2(b)$ optical emission at 762 nm. It was determined both radially averaged ($T_\mathrm{g,av}$) and radially resolved, with 1 mm resolution. The gas temperature near the wall (T_nw) was determined at 1 mm from the wall from High Resolution Two-photon Absorption Laser-Induced Fluorescence (HR TALIF) measurements of the Doppler profile of O atoms. Booth *et al* (2019) found from measurements and 1D radially-resolved calculations that T_nw is related to the other temperatures:

$$T_\mathrm{nw} \simeq T_\mathrm{w} + 0.28\left(T_\mathrm{g,av} - T_\mathrm{w}\right). \tag{1}$$

The atomic oxygen fraction was also measured for every condition via actinometry. This technique was also used to measure the temporal variations of O atom fraction during discharge modulation, from which is obtained the effective loss frequency of O atoms $\nu^\mathrm{O}_\mathrm{loss}$. From that measurement, the wall recombination coefficient of O (γ_O) is also obtained, employing the expression (Booth *et al* 2019):

$$\gamma_\mathrm{O} = \left(\nu^\mathrm{O}_\mathrm{loss} - L_\mathrm{av}\right) \cdot \frac{2R_\mathrm{tube}}{v_\mathrm{th,O}} \cdot \frac{[\mathrm{O}]_\mathrm{av}}{[\mathrm{O}]_\mathrm{nw}}, \tag{2}$$

where L_av is the average volume loss rate of O, R_tube is the tube radius of 1 cm, $[\mathrm{O}]_\mathrm{av}$ is the average O atom density and $[\mathrm{O}]_\mathrm{nw}$ is its near-wall value. $v_\mathrm{th,O}$ is the thermal velocity of O calculated as:

$$v_\mathrm{th,O} = \sqrt{\frac{8k_\mathrm{B}T_\mathrm{nw}}{\pi M_\mathrm{O}}}, \tag{3}$$

where k_B is the Boltzmann constant and M_O is the mass of the O atom. Booth *et al* (2019) calculated $\frac{[\mathrm{O}]_\mathrm{av}}{[\mathrm{O}]_\mathrm{nw}}$ from 1D model results of $T_\mathrm{g}(r)$ and the assumption that the O atom density profile follows the total gas density, determined from the ideal gas law, which is reported to induce up to a 30% decrease of γ_O with respect to the case considering $[\mathrm{O}]_\mathrm{av} = [\mathrm{O}]_\mathrm{nw}$. L_av was computed by considering only the three body recombination of two atoms with rate coefficient $k = 3.34 \times 10^{-30} \cdot (1/T_\mathrm{g,av}) \cdot \mathrm{e}^{-170/T_\mathrm{g,av}}\ \mathrm{cm}^6 \cdot \mathrm{s}^{-1}$, which results in L_av being reported as less than 10% of $\nu^\mathrm{O}_\mathrm{loss}$. The resulting γ_O values were shared by Booth *et al* (2019) with the current authors and are represented in figure 2 for the two different wall temperatures.

2.2. Experimental data at different wall temperatures: data set 2

Data set 2 was obtained by Dias (2019) in a similar set-up as data set 1, with the same dimensions and characteristics, but in a different tube and measurement campaign. It contains a total of 50 conditions: 11 for $T_\mathrm{w} = -20\,^\circ\mathrm{C}$, 13 for $T_\mathrm{w} = 5\,^\circ\mathrm{C}$, 13 for $T_\mathrm{w} = 25\,^\circ\mathrm{C}$ and 13 for $T_\mathrm{w} = 50\,^\circ\mathrm{C}$. These include pressure values of 0.8, 1, 1.5, 2, 3, 5 and 7.5 Torr and currents of 20 and 40 mA. The gas temperature was measured in the same way as by Booth *et al* (2019) for $T_\mathrm{w} = 5\,^\circ\mathrm{C}$ and $T_\mathrm{w} = 50\,^\circ\mathrm{C}$. For the remaining wall temperatures, $T_\mathrm{g,av}$ was calculated assuming a linear dependence of $T_\mathrm{g,av}$ with T_w. T_nw was then obtained from equation (1). The atomic oxygen density was measured via actinometry and its temporal variation was obtained from the temporal evolution of line emission intensity ratios, which led to obtaining the effective loss frequency of O atoms $\nu^\mathrm{O}_\mathrm{loss}$.

In this work, γ_O for data set 2 is calculated from equation (2), by taking the approximation $[\mathrm{O}]_\mathrm{av}/[\mathrm{O}]_\mathrm{nw} = 1$, and calculating L_av as was done by Booth *et al* (2019) for data set 1. It should be noticed that in the work by Viegas

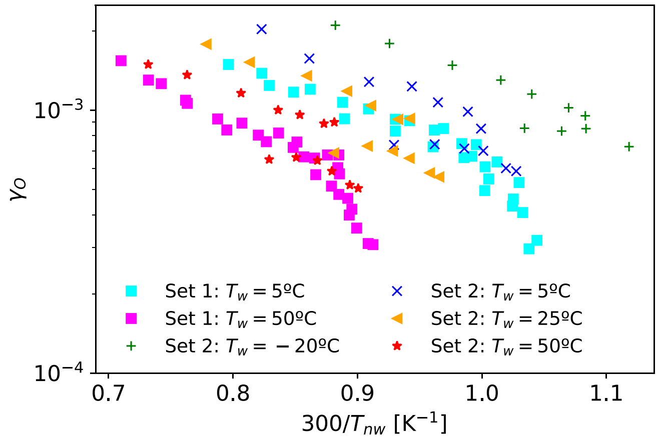

Figure 2. O atom wall loss probability in Pyrex as function of the reverse of the near-wall temperature, for different wall temperatures. Results from experimental measurements from data set 1 (Booth *et al* 2019) and data set 2.

et al (2023) it was concluded, based on 1D simulation results, that it may be more accurate to assume radially uniform O density ($[\mathrm{O}]_{\mathrm{nw}} = [\mathrm{O}]_{\mathrm{av}}$) than to assume proportionality with gas density and thus with the inverse of gas temperature ($[\mathrm{O}]_{\mathrm{nw}} = [\mathrm{O}]_{\mathrm{av}} \cdot T_{\mathrm{g,av}}/T_{\mathrm{nw}}$), which assumes a radial uniformity of source and loss rates of O atoms that is not verified (figure 4 in that work). The consideration of L_{av}, instead of assuming $L_{\mathrm{av}} \simeq 0$, induces a difference in γ_{O} of up to 21.5%, although of only 5% on average.

The resulting γ_{O} of data set 2 are represented in figure 2, for the different wall temperatures, together with those of data set 1. Considering the significant amount of data and of pressure and current conditions, in this work the γ_{O} values are represented, in either logarithmic or linear scale, for different wall temperatures as function of the inverse of the gas temperature near the wall, as $\gamma_{\mathrm{O}} = f(300/T_{\mathrm{nw}})$. We believe this way of plotting the data is the one that best represents the direct dependences of γ_{O}. We should notice that T_{nw} always increases with T_{w}, pressure and current in the studied range of conditions (Booth *et al* 2019, 2022, Dias 2019).

Figure 2 shows not only the decrease of γ_{O} with T_{w} and T_{nw}, but also the similarity between γ_{O} from data sets 1 and 2 for $T_{\mathrm{w}} = 5\,^{\circ}\mathrm{C}$ and $T_{\mathrm{w}} = 50\,^{\circ}\mathrm{C}$, even though the data was obtained in different tubes. Nevertheless, the data exhibit an uncertainty in reproducibility of up to 39% between the two sets. We should notice that this difference between data sets 1 and 2 is much lower than that reported by Booth *et al* (2020) where for similar conditions $\nu^{\mathrm{O}}_{\mathrm{loss}}$ can be more than double of the one measured by Booth *et al* (2019), which is attributed to different Pyrex tube histories (Cartry *et al* 1999). In the remaining figures in this work, an errorbar is represented to take into account the experimental uncertainty of γ_{O}. Taking into account that the uncertainty of measurement is low and the uncertainty in the conversion of $\nu^{\mathrm{loss}}_{\mathrm{O}}$ to γ_{O} is of the order of $L_{\mathrm{av}}/\nu^{\mathrm{O}}_{\mathrm{loss}} \simeq 5\%$, we consider that the experimental uncertainty is mostly due to reproducibility. To guide the eye, we add a 30% error bar to γ_{O} measured in experiments.

3. Surface kinetics model

The mechanisms taking place at the surface are effectively taken into account via a mesoscopic (not atomistic) description (Kim and Boudart 1991, Guerra 2007, Guerra and Marinov 2016, Marinov *et al* 2017). In this model, the Pyrex surface is considered fully covered by a series of adsorption sites, which can reversibly or irreversibly hold O atoms and $\mathrm{O_2}$ molecules incoming from the $\mathrm{O_2}$ plasma, where dissociation takes place. Reversible adsorption is associated with physisorption, at surface sites $\mathrm{F_V}$ of total density [F], in which the bond between the particle and the surface is due to van der Waals forces. Due to their relatively low energy bonds, physisorbed atoms $\mathrm{O_F}$ or molecules $\mathrm{O_{2,F}}$ can diffuse along the surface or desorb back to the gas phase. Physisorption can occur at any site on the surface. Conversely, chemisorption identifies irreversible adsorption, where a true chemical bond (covalent or ionic bond) exists between the adsorbed atom and the surface. It takes place on surface defects $\mathrm{S_V}$ of total density [S], where the bonds with O are promoted. Due to the high energy of the bond and the lack of sufficiently high temperatures to promote thermal desorption below ≃2000 K (Kim and Boudart 1991), it is assumed that a chemisorbed atom $\mathrm{O_S}$ can only leave the surface site through recombination with another O atom. In reality, there may be a distribution of bonding energies for species adsorbed at the surface (Marinov *et al* 2017). As a simplification, we consider only two types of adsorbed species: physisorbed with zero energy bond and chemisorbed with relatively high energy bond. In this work, different sets of reactions and parameters are taken, which are summarized in the next subsections. The considered processes generally include physisorption, thermal desorption from physisorption sites, chemisorption, E-R recombination between a gas-phase and an adsorbed species, chemisorption via surface diffusion of physisorbed atoms, and L-H recombination between two adsorbed species.

In this work the deterministic method is numerically employed for different reaction schemes, as explained by Marinov *et al* (2017) and recently recalled by Afonso *et al* (2024). Through the deterministic method, a system of rate balance equations is solved for the surface densities n_i of every species i. For reactions j with only one surface reactant k (e.g. R1-R5 in table 1), the model solves:

$$\left.\frac{\mathrm{d}n_i}{\mathrm{d}t}\right|_{(I)} = \sum_j \left(c^R_{i,j} - c^L_{i,j}\right) S_j = \sum_j \left(c^R_{i,j} - c^L_{i,j}\right) n_k r_j, \qquad (4)$$

where $c^R_{i,j}$ and $c^L_{i,j}$ are the stoichiometric coefficients of species i in reaction j on the right-hand side (production) and left-hand (destruction) side of the reaction equation, respectively, S_j is the corresponding source or loss term and r_j is the rate of reaction j in units of site$^{-1}\cdot$s^{-1}. For reactions j where there is one surface reactant $\mathrm{O_F}$ and one surface reactant k (e.g. R6-R8 in table 3), the rate balance equations are solved as:

$$\left.\frac{\mathrm{d}n_i}{\mathrm{d}t}\right|_{(II)} = \sum_j \left(c^R_{i,j} - c^L_{i,j}\right) S_j = \sum_j \left(c^R_{i,j} - c^L_{i,j}\right) \theta_{\mathrm{F}} n_k r_j, \qquad (5)$$

where $\theta_\mathrm{F} = [\mathrm{O_F}]/[\mathrm{F}]$ is the fractional coverage of $\mathrm{O_F}$. Then:

$$\frac{\mathrm{d}n_i}{\mathrm{d}t} = \left.\frac{\mathrm{d}n_i}{\mathrm{d}t}\right|_{(I)} + \left.\frac{\mathrm{d}n_i}{\mathrm{d}t}\right|_{(II)}. \tag{6}$$

Finally, the recombination probability is calculated in this model as in the works by Guerra (2007) and Marinov *et al* (2017), as the quotient from dividing the surface recombination rate (written as in equations (4) and (5), including the multiplication by the number of recombining O atoms per recombination reaction) by the incoming flux of atoms to the surface, such that:

$$\gamma_\mathrm{O} = \gamma_\mathrm{O+O} + \gamma_\mathrm{O+O_2} = \frac{2\sum_j S_\mathrm{j,O+O}}{\phi_\mathrm{O}} + \frac{\sum_j S_\mathrm{j,O+O_2}}{\phi_\mathrm{O}}, \tag{7}$$

where ϕ_O is the thermal flux of incoming O atoms from the gas phase to the surface.

In the works by Guerra and Loureiro (2004), Guerra and Marinov (2016), Marinov *et al* (2017)and Afonso *et al* (2024), another method is used to solve the system of surface reactions, the Kinetic Monte Carlo (KMC) method. Instead of dealing with average surface coverages the KMC method follows every particle and every site on the surface. Therefore, using KMC, the state of the system can be described as a list of all active sites in the simulation domain together with their occupancies, evolving in time according to the listed reactions and their probabilities. As explained in the works by Guerra and Marinov (Guerra and Marinov 2016, Marinov *et al* 2017), KMC allows to obtain more accurate results than the deterministic method that takes approximations concerning the diffusion of physisorbed species. In this work, KMC is not employed, since the studied conditions are similar to those in the works by Marinov *et al* (2017) and by Afonso *et al* (2024), where it was confirmed that the KMC and deterministic results are close, within a 20% difference.

The input required for the model from the experimental data sets are pressure, T_g, T_w and $[\mathrm{O}]_\mathrm{av}$. T_nw is calculated from equation (1) and $[\mathrm{O_2}]_\mathrm{av}$ is obtained approximately as $[\mathrm{O_2}]_\mathrm{av} \simeq N - [\mathrm{O}]_\mathrm{av}$, where N is the gas density calculated from the ideal gas law. The thermal fluxes of incoming O and $\mathrm{O_2}$ particles from the gas phase to the surface are calculated as:

$$\phi_\mathrm{O} = \frac{1}{4}[\mathrm{O}]_\mathrm{av} v_\mathrm{th,O}, \tag{8}$$

$$\phi_\mathrm{O_2} = \frac{1}{4}[\mathrm{O_2}]_\mathrm{av} v_\mathrm{th,O_2}, \tag{9}$$

where v_th are the thermal velocities calculated as in equation (3). As noticed in the work by Viegas *et al* (2023), near the wall it may be more accurate to assume $[\mathrm{O}]_\mathrm{nw} = [\mathrm{O}]_\mathrm{av}$, as in this work, than to consider $[\mathrm{O}]_\mathrm{nw} = [\mathrm{O}]_\mathrm{av} \cdot T_\mathrm{g,av}/T_\mathrm{nw}$. Nevertheless, it was verified that the impact of changing that assumption is very subtle in the conditions under study. The following subsections describe the different reaction sets and kinetic data employed in the surface kinetics model.

3.1. Reaction set from Booth et al (2019)

Based on the experimental results of data set 1 (see figure 2), Booth *et al* (2019) analysed that, for each value of T_w, for pressure above 2 Torr, the logarithm of γ_O falls linearly with $300/T_\mathrm{nw}$, which constitutes an Arrhenius behaviour. According to Booth *et al* (2019), this suggests that recombination is dominated by E-R processes that depend on the energy of incoming atoms, and thus on T_nw, and not by L-H mechanisms involving diffusing physisorbed atoms, whose rates only depend on T_w, and thus whose γ_O contribution should be constant for a fixed T_w. Booth *et al* (2019) further noticed that the data points for low T_nw (pressures below 2 Torr) do not lie on the Arrhenius line and instead there is a ‘knee’ in the Arrhenius plot (in figure 2, more visible for data set 1 than for data set 2). Moreover, they assessed that the decrease of γ_O with T_w for the same T_nw implies a varying occupation of sites with T_w. Both factors suggest an involvement of physisorbed atoms. Based on this evaluation, Booth *et al* (2019) suggested an effective reaction set describing the atomic oxygen recombination in a simple way. Their aim was to propose a phenomenological but robust surface reaction model with a small number of adjustable parameters, validated against well-defined measurements (data set 1), thus minimizing the arbitrariness of their values. The list of proposed reactions is presented in table 1, along with the corresponding rates. The description of parameters is given in table 2. The list includes physisorption (R1), desorption (R2), chemisorption (R3) and E-R recombination with chemisorbed (R4) and physisorbed (R5) atoms.

In this work, the system is solved analytically but also employing the mathematical framework previously described (equations (4)–(6)). For the approximate analytical solution, equations (19) and (26) from the work by Booth *et al* (2019) are used:

$$\gamma_\mathrm{O+O_S} = \frac{2R}{v_\mathrm{th}} k_3^0 P_4^0 [\mathrm{S}] \cdot \exp\left(-\frac{E_\mathrm{ER}^S}{RT_\mathrm{nw}}\right), \tag{10}$$

$$\gamma_\mathrm{O+O_F} = \frac{2R}{v_\mathrm{th}} k_1^0 P_5^0 [\mathrm{F}] \cdot \exp\left(-\frac{E_\mathrm{ER}^F}{RT_\mathrm{nw}}\right) \cdot \frac{[\mathrm{O}]_\mathrm{nw} \cdot (R/2)}{\left(\nu_\mathrm{d} \cdot \exp\left(-\frac{E_\mathrm{d}}{RT_\mathrm{w}}\right)/k_1^0\right)}, \tag{11}$$

$$\gamma_\mathrm{O} = \gamma_\mathrm{O+O_S} + \gamma_\mathrm{O+O_F}. \tag{12}$$

It should be noticed that the multiplication by $R/2$ in equation (11) is not presented in equation (26) in the work by Booth *et al* (2019) but was deemed necessary and added in this work. Concerning the numerical solution, the process rates are taken from Booth *et al* (2019) but written differently, in a compatible way with our mathematical formulation. For the choice of parameters, Booth *et al* (2019) considered two extreme cases regarding the activation energy for recombination: in case 1 the activation energies for E-R recombination are the same for chemisorbed and physisorbed O atoms ($E_\mathrm{ER}^S = E_\mathrm{ER}^F$), which would mean that the activation energy depends only on the interaction between the adsorbed atom and the gas phase atom, and is independent of the nature of the bond between

Table 1. List of surface reactions in the model from Booth *et al* (2019). V and S, respectively, are the volume and the surface of the reactor ($V/S = R_{\mathrm{tube}}/2$). $[\mathrm{O}]_{\mathrm{nw}} = [\mathrm{O}]_{\mathrm{av}} \cdot T_{\mathrm{g,av}}/T_{\mathrm{nw}}$ is the estimated density of O atoms near the wall. R is the ideal gas constant, T_{w} is the wall temperature and T_{nw} is the near-wall temperature.

Nbr.	Reaction	Rate [$\mathrm{site}^{-1} \cdot \mathrm{s}^{-1}$]
R1	$\mathrm{O(g)} + \mathrm{F_V} \rightarrow \mathrm{O_F}$	$r_1 = k_1^0 \cdot [\mathrm{O}]_{\mathrm{nw}} \cdot \frac{V}{S}$
R2	$\mathrm{O_F} \rightarrow \mathrm{O(g)} + \mathrm{F_V}$	$r_2 = \nu_d \cdot \exp\left(-\frac{E_d}{RT_{\mathrm{w}}}\right)$
R3	$\mathrm{O(g)} + \mathrm{S_V} \rightarrow \mathrm{O_S}$	$r_3 = k_3^0 \cdot [\mathrm{O}]_{\mathrm{nw}} \cdot \frac{V}{S}$
R4	$\mathrm{O(g)} + \mathrm{O_S} \rightarrow \mathrm{O_2(g)} + \mathrm{S_V}$	$r_4 = r_3 \times P^S_{\mathrm{ER}}, P^S_{\mathrm{ER}} = P_4^0 \cdot \exp\left(-\frac{E^S_{\mathrm{ER}}}{RT_{\mathrm{nw}}}\right)$
R5	$\mathrm{O(g)} + \mathrm{O_F} \rightarrow \mathrm{O_2(g)} + \mathrm{F_V}$	$r_5 = r_1 \times P^F_{\mathrm{ER}}, P^F_{\mathrm{ER}} = P_5^0 \cdot \exp\left(-\frac{E^F_{\mathrm{ER}}}{RT_{\mathrm{nw}}}\right)$

Table 2. List of parameters in the model from Booth *et al* (2019) (case 1 in that work). It is found in this work that P_4^0 and P_5^0 should be divided by 2 ($P_4^0 = P_5^0 = 0.022$) for coherence purposes with the definition of γ_{O} in equation (7), as explained in the text.

Parameter	Description	Value
[F]	Density of physisorption sites	$1.0 \times 10^{20}\ \mathrm{m}^{-2}$
[S]	Density of chemisorption sites	$1.5 \times 10^{18}\ \mathrm{m}^{-2}$
φ	Fraction of chemisorption sites	1.5×10^{-2}
k_1^0, k_3^0	Effective rate constant of gas-surface atom collision	$2 \times 10^{-14}\ \mathrm{m}^2 \cdot \mathrm{s}^{-1}$
P_4^0, P_5^0	Pre-exponential factor for recombination	0.044
ν_{d}	Pre-exponential factor of desorption frequency	$10^{13}\ \mathrm{s}^{-1}$
E_{d}	Desorption barrier	$29.1\ \mathrm{kJ} \cdot \mathrm{mol}^{-1}$
E^S_{ER}	Recombination barrier for E-R with chemisorbed	$12.5\ \mathrm{kJ} \cdot \mathrm{mol}^{-1}$
E^F_{ER}	Recombination barrier for E-R with physisorbed	$12.5\ \mathrm{kJ} \cdot \mathrm{mol}^{-1}$

the adsorbed atom and the surface; in case 2 the E-R recombination with physisorbed atoms is considered to have zero activation energy ($E^F_{\mathrm{ER}} = 0$), which corresponds to considering that the activation energy depends on the bond between the adsorbed atom and the surface, which is much lower for physisorbed than chemisorbed atoms (Kim and Boudart 1991, Guerra 2007, Marinov *et al* 2017). A clarification on the nature of the activation energy for recombination should resort to DFT and/or molecular dynamics calculations and falls outside the scope of this work. For each case, the obtained analytical expressions of γ_{O} were used by Booth *et al* (2019) to fit the experimental results of data set 1. The recombination barriers, the desorption barrier and the recombination reaction probability were obtained from those fits. The parameters used in case 1 in the model by Booth *et al* (2019) are listed in table 2.

The numerical calculations employing the surface kinetics model in this work and the reactions, rates and parameters of tables 1 and 2 are compared to the approximate analytical solution and the experimental results in figure 3, for $T_{\mathrm{w}} = 5\,^{\circ}\mathrm{C}$ (figure 3(a)) and for $T_{\mathrm{w}} = 50\,^{\circ}\mathrm{C}$ (figure 3(b)). The contributions of the two E-R recombination mechanisms are also represented. The same type of figure was shown by Booth *et al* (2019), employing the analytical calculations (figures 11 and 12 in that work). As shown by Booth *et al* (2019), the calculated γ_{O} obtained from 'case 2' parameters would be similar to the ones shown here ('case 1'), although with different contributions to recombination from E-R with chemisorbed and E-R with physisorbed O atoms. Booth *et al* (2019) found the fitting parameters of table 1 by considering $\gamma_{\mathrm{O}} = \sum_j S_{\mathrm{j,O+O}}/\phi_{\mathrm{O}}$ (equations (18) and (25) in that work), instead of the loss probability $\gamma_{\mathrm{O}} = 2\sum_j S_{\mathrm{j,O+O}}/\phi_{\mathrm{O}}$ (equation (7) in this work). For that reason, there is necessarily a factor 2 difference between our model simulations employing the given parameters and the experimental γ_{O}. In figure 3 the simulation results are divided by 2 to provide an appropriate comparison. It should be noticed that the same result is obtained by dividing the pre-exponential factor for recombination by 2, which is what might have been found from the fits by Booth *et al* (2019) if equation (7) had been used to define γ_{O}. The accuracy of these statements is confirmed in figure 3, where the match between the analytical and numerical solutions is shown. This match means that the analytical expressions given by Booth *et al* (2019) are very closely retrieved by taking in our deterministic numerical model the mechanisms suggested in that paper with the rate coefficients proposed.

Figure 3 shows that the phenomenological model by Booth *et al* (2019) effectively correctly describes the experimental trends of γ_{O}, with the curvature in the $\gamma_{\mathrm{O}} = f(300/T_{\mathrm{nw}})$ dependence evincing a key role of physisorbed O atoms, which is accounted in a simplified way through O + $\mathrm{O_F}$ recombination. However, the actual picture may be more complex and this may correspond to an effective way of describing a sequence of elementary steps (Booth *et al* 2019). In this work, we intend to provide a description of surface kinetics that accurately depicts the more complex physical picture of O recombination, not fully represented in the model by Booth *et al* (2019). Indeed, if all the expected recombination processes were included, namely L-H recombination, the

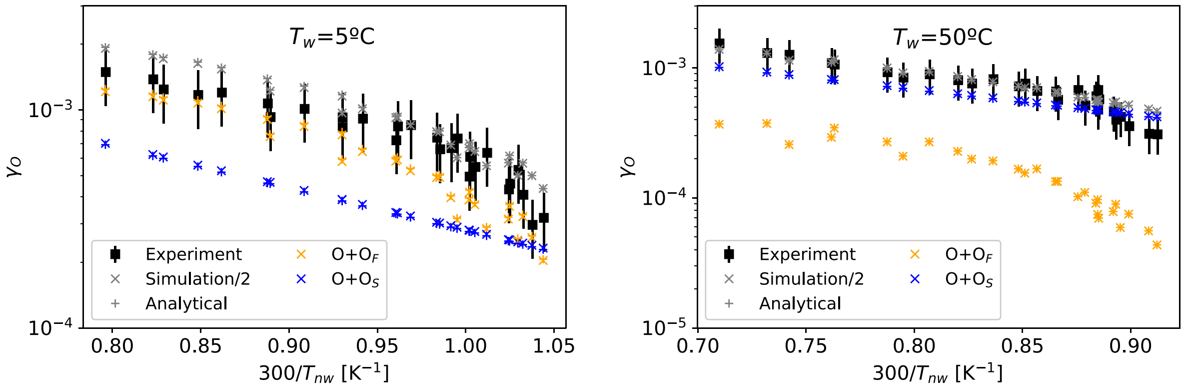

(a) (b)

Figure 3. O atom wall loss probability in Pyrex as function of the reverse of the near-wall temperature, for (a) $T_w = 5\,^\circ$C and (b) $T_w = 50\,^\circ$C. Results from experimental measurements from data set 1 (Booth *et al* 2019) and from analytical and numerical calculations employing the reaction set from Booth *et al* (2019) (case 1 in that work). The numerical simulation results are divided by 2 for reasons explained in the text. The calculations presented include the total γ_O ($\times$ and $+$) and the contributions of the different recombination mechanisms.

Table 3. List of surface reactions in the base model (Marinov *et al* 2017). ϕ_O is the thermal flux of gas-phase O (O(g)) to the wall (equation (8)), R is the ideal gas constant, T_w is the wall temperature and T_{nw} is the near-wall temperature.

Nbr.	Reaction	Rate [site$^{-1}\cdot$s^{-1}]
R1	$O(g) + F_V \rightarrow O_F$	$r_1 = \frac{P_1^0}{[F]+[S]}\phi_O$
R2	$O_F \rightarrow O(g) + F_V$	$r_2 = \nu_d \cdot \exp\left(-\frac{E_d}{RT_w}\right)$
R3	$O(g) + S_V \rightarrow O_S$	$r_3 = \frac{P_3^0}{[F]+[S]}\phi_O$
R4	$O(g) + O_S \rightarrow O_2(g) + S_V$	$r_4 = r_3 \times P_{ER}^S, P_{ER}^S = P_4^0 \cdot \exp\left(-\frac{E_{ER}^S}{RT_{nw}}\right)$
R6	$O_F + S_V \rightarrow F_V + O_S$	$r_6 = \frac{3}{4} \times \tau_D^{-1}, \tau_D^{-1} = \nu_D \cdot \exp\left(-\frac{E_D}{RT_w}\right) \frac{[F]}{[F]+[S]}$
R7	$O_F + O_S \rightarrow O_2(g) + F_V + S_V$	$r_7 = P_{LH}^S \times \tau_D^{-1}, P_{LH}^S = P_7^0 \cdot \exp\left(-\frac{E_{LH}^S}{RT_w}\right)$
R8	$O_F + O_F \rightarrow O_2(g) + F_V + F_V$	$r_8 = 2 \times P_{LH}^F \times \tau_D^{-1}, P_{LH}^F = P_8^0 \cdot \exp\left(-\frac{E_{LH}^F}{RT_w}\right)$

simulated γ_O in figure 3 would be up to two orders of magnitude higher, as shown by Morillo-Candás (2019) (figure 8.25 in that work). This is due especially to the low value of ν_d (10^{13} s^{-1}) taken by Booth *et al* (2019), that would guarantee a high population of physisorbed atoms (between 10^{-3} and 3×10^{-2} in the calculations of figure 3). To provide such a more accurate description, we start by presenting our base model, employed in previous works, and then we build on it towards an upgraded model.

3.2. Base reaction set

The base model considered in this work is the one by Marinov *et al* (2017), based on the works by Kim and Boudart (1991), Guerra (2007)and Guerra and Marinov (2016), and recently extended to low pressures by Afonso *et al* (2024). The base model is represented in terms of reactions and rates in table 3, with the corresponding parameters listed in table 4. It is a model for O atom adsorption and recombination that includes physisorption (R1), desorption (R2), chemisorption (R3), E-R recombination with O_S (R4), chemisorption via surface diffusion of O_F (R6) and L-H recombination with O_S (R7) and with O_F (R8). We should notice that E-R recombination with O_F (R5 in table 1) is not part of this base model. On the one hand, the bond between physisorbed atoms and the surface is relatively weak, so that recombination involving a physisorbed atom can be relatively easy. On the other hand, if the kinetic energy of the atoms arriving to the surface is relatively high, physisorbed atoms may be removed from the surface by the impingement of gas phase atoms, without recombining, or the incoming atoms may escape the potential well and proceed towards the closest O_S. None of these processes are taken into account in the base model, with the atoms arriving from the gas phase to an occupied physisorption site being assumed to simply reflect (Guerra 2007).

The rates considered in table 3 are explained in the work by Guerra (2007). However, in this work, as in the works by Booth *et al* (2019) and Guerra *et al* (2019), the kinetic energy of incoming particles from the gas phase is considered, by taking T_{nw} instead of T_w in the rates involving those particles

Table 4. List of parameters in the base model (Marinov *et al* 2017).

Parameter	Description	Value
[F]	Density of physisorption sites	1.5×10^{19} m^{-2}
[S]	Density of chemisorption sites	3.0×10^{17} m^{-2}
φ	Fraction of chemisorption sites	2×10^{-2}
P_1^0	Sticking probability for physisorption	1
P_3^0	Sticking probability for chemisorption	1
P_4^0, P_7^0, P_8^0	Pre-exponential factors for recombination	1
ν_d	Pre-exponential factor of desorption frequency	10^{15} s^{-1}
ν_D	Pre-exponential factor of diffusion frequency	10^{13} s^{-1}
E_d	Desorption barrier	30 kJ $\cdot$ mol^{-1}
E_D	Diffusion barrier	15 kJ $\cdot$ mol^{-1}
E_ER^S	Recombination barrier for E-R with chemisorbed	17.5 kJ $\cdot$ mol^{-1}
E_LH^S	Recombination barrier for L-H with chemisorbed	17.5 kJ $\cdot$ mol^{-1}
E_LH^F	Recombination barrier between physisorbed atoms	0

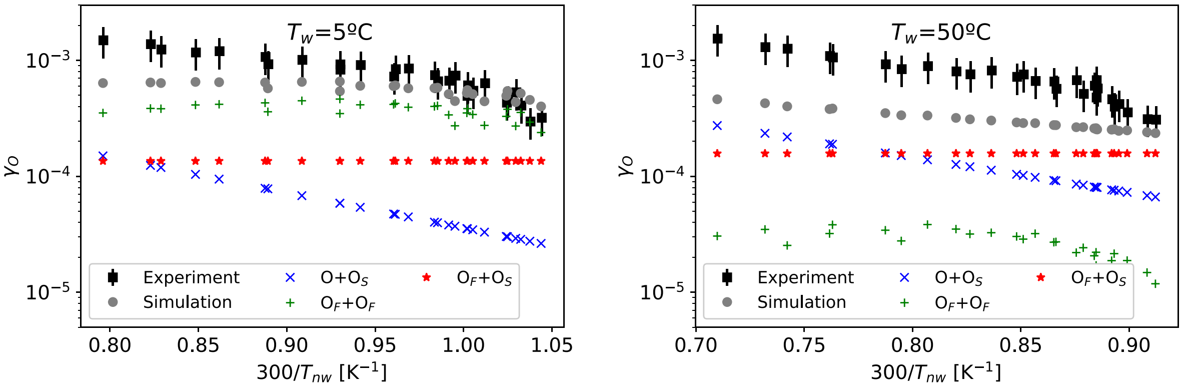

(a) (b)

Figure 4. O atom wall loss probability in Pyrex as function of the reverse of the near-wall temperature, for (a) $T_\mathrm{w} = 5\,^\circ$C and (b) $T_\mathrm{w} = 50\,^\circ$C. Results from experimental measurements from data set 1 (Booth *et al* 2019) and from simulations employing the base model. The simulation results presented include the total γ_O (●) and the contributions of the different recombination mechanisms.

(adsorption and E-R recombination). The parameters in table 4 were picked in the work by Guerra and Marinov (2016), based on previous studies of O recombination in SiO$_2$ surfaces (Kim and Boudart 1991, Seward and Jumper 1991, Gordiets and Ferreira 1998, Cartry *et al* 2000, Guerra 2007, Lopaev *et al* 2011a) and on the agreement with previous experiments (shown in figure 7 in that work). That work includes a discussion of the uncertainties of the chosen parameters, through comparisons with those considered in other works. The different ways to obtain surface parameters were also discussed in the work by Marinov *et al* (2017), pointing out that these can be obtained from ab-initio calculations, direct measurement, tuning to match experimental measurements and 'guesstimation'. It was concluded that even in such a relatively simple system consisting of only two chemical elements, oxygen and silicon, a significant uncertainty still remains, with the recombination mechanisms themselves not being fully understood. As such, this base model, as other mesoscopic models, remains an effective way to account for complex phenomena only through a few reactions and parameters. In figure 4, the base model simulation results of γ_O are compared to the data set 1 experimental measurements, for $T_\mathrm{w} = 5\,^\circ$C and $T_\mathrm{w} = 50\,^\circ$C. The contributions of the three different recombination mechanisms are also presented.

Figure 4(a) shows that, at $T_\mathrm{w} = 5\,^\circ$C, the base model simulation results are close to the experiments, with the dominant recombination mechanism being L-H recombination between physisorbed atoms. This mechanism provides a visible curvature, in agreement with experiments. Nevertheless, it is visible that at $T_\mathrm{w} = 5\,^\circ$C and high T_nw ($300/T_\mathrm{nw} < 0.9$) the steepness of the simulation trend and the experimental trend are different, which suggests there should be a stronger role of the O+O$_\mathrm{S}$ recombination mechanism in those conditions. Despite the agreement at $T_\mathrm{w} = 5\,^\circ$C, figure 4(b) shows that the simulation results are farther from reproducing the measurements at $T_\mathrm{w} = 50\,^\circ$C. In this case, the simulated γ_O is lower than the experimental results, up to a factor 4, and is given mostly by O+O$_\mathrm{S}$ and O$_\mathrm{F}$+O$_\mathrm{S}$ recombination mechanisms, which cannot provide the curvature observed in experiments. This analysis suggests that recombination processes providing the curvature, such as O$_\mathrm{F}$+O$_\mathrm{F}$ or O+O$_\mathrm{F}$ (see figure 3), should have a more prominent role than that attributed in the base model. Following the discussion by Guerra and Marinov (2016), we should notice that, of all the parameters of table 4,

Table 5. List of surface reactions in the upgraded model. ϕ_O is the thermal flux of gas-phase O (O(g)) to the wall (equation (8)), ϕ_{O_2} is the thermal flux of gas-phase O_2 (O_2(g)) to the wall (equation (9)), R is the ideal gas constant, T_w is the wall temperature and T_{nw} is the near-wall temperature. Reactions R1-R8 are the same as presented in tables 1 and 3, while reactions R9-R15 are new.

Nbr.	Reaction	Rate ($\text{site}^{-1} \cdot \text{s}^{-1}$)
R1	$O(g) + F_V \rightarrow O_F$	$r_1 = \frac{P_1^0}{[F]+[S]} \phi_O$
R2	$O_F \rightarrow O(g) + F_V$	$r_2 = \nu_d \cdot \exp\left(-\frac{E_d^O}{RT_w}\right)$
R3	$O(g) + S_V \rightarrow O_S$	$r_3 = \frac{P_3^0}{[F]+[S]} \phi_O$
R4	$O(g) + O_S \rightarrow O_2(g) + S_V$	$r_4 = r_3 \times P_{ER}^S, P_{ER}^S = P_4^0 \cdot \exp\left(-\frac{E_{ER}^S}{RT_{nw}}\right)$
R5	$O(g) + O_F \rightarrow O_2(g) + F_V$	$r_5 = r_1 \times P_{ER}^F, P_{ER}^F = P_5^0 \cdot \exp\left(-\frac{E_{ER}^F}{RT_{nw}}\right)$
R6	$O_F + S_V \rightarrow F_V + O_S$	$r_6 = \frac{3}{4} \times \tau_D^{-1}, \tau_D^{-1} = \nu_D \cdot \exp\left(-\frac{E_D}{RT_w}\right) \frac{[F]}{[F]+[S]}$
R7	$O_F + O_S \rightarrow O_2(g) + F_V + S_V$	$r_7 = P_{LH}^S \times \tau_D^{-1}, P_{LH}^S = P_7^0 \cdot \exp\left(-\frac{E_{LH}^S}{RT_w}\right)$
R8	$O_F + O_F \rightarrow O_2(g) + F_V + F_V$	$r_8 = 2 \times P_{LH}^F \times \tau_D^{-1}, P_{LH}^F = P_8^0 \cdot \exp\left(-\frac{E_{LH}^F}{RT_w}\right)$
R9	$O_2(g) + F_V \rightarrow O_{2,F}$	$r_9 = \frac{P_9^0}{[F]+[S]} \phi_{O_2}$
R10	$O_{2,F} \rightarrow O_2(g) + F_V$	$r_{10} = \nu_d \cdot \exp\left(-\frac{E_d^{O_2}}{RT_w}\right)$
R11	$O_2(g) + O_F \rightarrow O_3(g) + F_V$	$r_{11} = r_9 \times P_{ER}^{O_2+O_F}, P_{ER}^{O_2+O_F} = P_{11}^0 \cdot \exp\left(-\frac{E_{ER}^{O_2+O_F}}{RT_{nw}}\right)$
R12	$O_2(g) + O_{2,F} \rightarrow O_2(g) + O_2(g) + F_V$	$r_{12} = r_9 \times P_{ER}^{O_2+O_{2,F}}, P_{ER}^{O_2+O_{2,F}} = P_{12}^0 \cdot \exp\left(-\frac{E_{ER}^{O_2+O_{2,F}}}{RT_{nw}}\right)$
R13	$O(g) + O_{2,F} \rightarrow O_3(g) + F_V$	$r_{13} = r_1 \times P_{ER}^{O+O_{2,F}}, P_{ER}^{O+O_{2,F}} = P_{13}^0 \cdot \exp\left(-\frac{E_{ER}^{O+O_{2,F}}}{RT_{nw}}\right)$
R14	$O_F + O_{2,F} \rightarrow O_3(g) + F_V + F_V$	$r_{14} = P_{LH}^F/\tau_D, P_{LH}^{O_F+O_{2,F}} = P_{14}^0 \cdot \exp\left(-\frac{E_{LH}^{O_F+O_{2,F}}}{RT_w}\right)$
R15	$O_{2,F} + O_F \rightarrow O_3(g) + F_V + F_V$	$r_{15} = P_{LH}^F/\tau_D, P_{LH}^{O_{2,F}+O_F} = P_{15}^0 \cdot \exp\left(-\frac{E_{LH}^{O_{2,F}+O_F}}{RT_w}\right)$

the pre-exponential factor of the desorption frequency ν_d is the most uncertain parameter, with values in literature between 10^{13} s^{-1} and 10^{16} s^{-1}, and may depend directly on T_w (Ibach *et al* 1980). These insights are valuable to develop an upgraded model that matches the experimental results through a more complete description of surface kinetics while keeping the simplicity of a mesoscopic model.

3.3. Upgraded reaction set

The reaction set developed in this work is based on the one presented by Guerra *et al* (2019) and on parametric studies by Morillo-Candás (2019) and Silveira (2023) and will be further presented in this section. It is summarized by the list of reactions and rates in table 5 and the list of parameters in table 6. In table 5, reactions R1-R8 are the same as presented earlier in tables 1 and 3, while reactions R9-R15 are new.

Starting from the base reaction set, the work by Guerra *et al* (2019) further considers O_2 physisorption (R9) and thermal desorption (R10) and the recombination between $O_{2,F}$ and O_F (R14,R15), to account for gaseous O_3 formation on the surface in the simplest possible way. The desorption energy for O_2 is taken in that work as 17.5 $kJ \cdot mol^{-1}$, close to the value of 18.3 $kJ \cdot mol^{-1}$ suggested by Lopaev *et al* (2011a) by matching experimental measurements in quartz (also a silica-like surface). This value is significantly lower than that considered for O, of 30 $kJ \cdot mol^{-1}$, also close to the value suggested by Lopaev *et al* (2011a) of 31.6 $kJ \cdot mol^{-1}$. It should be noticed that processes R14 and R15 are distinguished since we consider that in each case it is the first reactant that moves towards the second reactant, having to overcome the bonding energy of the second reactant to the surface. In this work, all the recombination processes involving weakly bonded atoms and no chemisorbed atoms are considered to have no energy barrier. For that reason, R14 and R15 end up having the same rate. Moreover, the diffusion and desorption frequencies are considered to be the same for O_F and $O_{2,F}$, as is the diffusion energy barrier. It is considered, as by Guerra *et al* (2019), that molecular chemisorption (into $O_{2,S}$) cannot take place because the distance between two neighbouring chemisorption sites is statistically too long to allow the simultaneous chemisorption at two surface sites. The chemisorption of one atom of an incoming molecule and the ejection of the other atom to the gas phase is also neglected.

Apart from the O+O_S and O_F+O_S recombination processes, the upgraded reaction set considers further recombination mechanisms involving physisorbed species. The possibility of L–H recombination between two physisorbed atoms

Table 6. List of parameters in the upgraded model. To distinguish new parameters from those already present in the base model, the mark (*) signals parameters modified in the upgraded model and the mark (#) signals parameters that are introduced as new in the upgraded model.

Parameter	Description	Value
[F]	Density of physisorption sites	1.5×10^{19} m^{-2}
[S]	Density of chemisorption sites	3×10^{17} m^{-2}
φ	Fraction of chemisorption sites	2×10^{-2}
P_1^0, P_9^0	Sticking probability for physisorption	1
P_3^0	Sticking probability for chemisorption	1
$P_4^0, P_5^0, P_7^0, P_8^0$	Pre-exponential factors for O-O recombination	1
$P_{11}^0 - P_{15}^0$ (#)	Pre-exponential factors for O_2 reactions	1
ν_d (*)	Pre-exponential factor of desorption frequency	$f(T_w)$
ν_D	Pre-exponential factor of diffusion frequency	10^{13} s^{-1}
E_d^O	Desorption barrier of O	30 kJ $\cdot$ mol^{-1}
$E_d^{O_2}$ (#)	Desorption barrier of O_2	17.5 kJ $\cdot$ mol^{-1}
E_D	Diffusion barrier	15 kJ $\cdot$ mol^{-1}
E_{ER}^S (*)	Recombination barrier for E-R with $O+O_S$	15.0 kJ $\cdot$ mol^{-1}
E_{ER}^F (*)	Recombination barrier for E-R with $O+O_F$	0
E_{LH}^S (*)	Recombination barrier for L-H with O_F+O_S	20.0 kJ $\cdot$ mol^{-1}
E_{LH}^F	Recombination barrier for L-H with O_F+O_F	0
$E_{ER}^{O_2+O_F}$ (#)	Recombination barrier for E-R with O_2+O_F	0
$E_{ER}^{O_2+O_{2,F}}$ (#)	Recombination barrier for E-R with $O_2+O_{2,F}$	0
$E_{ER}^{O+O_{2,F}}$ (#)	Recombination barrier for E-R with $O+O_{2,F}$	0
$E_{LH}^{O_F+O_{2,F}}$ (#)	Recombination barrier for E-H with $O_F+O_{2,F}$	0
$E_{LH}^{O_{2,F}+O_F}$ (#)	Recombination barrier for L-H with $O_{2,F}+O_F$	0

(R8) was considered in the work by Rakhimova *et al* (2009) and was discussed and included already in the works by Guerra and Loureiro (2004), Guerra and Marinov (2016), Marinov *et al* (2017), Alves *et al* (2018), Guerra *et al* (2019), where it was found to be one of the dominant mechanisms. E–R recombination involving weakly bonded atoms is not included in the base reaction set of table 3, but is put in evidence in the works by Lopaev *et al* (2011a, 2011b)and by Booth *et al* (2019). This mechanism (R5) is included in the upgraded set for the sake of completion. E-R recombination mechanisms resulting in ozone formation (R11 and R13) are also considered. These mechanisms were proposed by Lopaev *et al* (2011a, 2011b) and by Marinov *et al* (2013b) and in those works constitute some of the main mechanisms for O surface recombination and efficient paths for ozone production in the pressure range between 10 and 50 Torr. They allowed to explain the high ozone concentrations observed in experiments that could not be explained only by gas-phase processes. The rates of these processes are written in this work following an analogy with other E-R rates, considering probability 1 of recombination interactions. Recently, the works by Meyer *et al* (2023) and by Booth *et al* (2023) also include considerations on O_3 surface production. Meyer *et al* (2023), with a coupled volume and surface kinetics model for a borosilicate glass (Pyrex) surface, included collision-induced desorption of $O_{2,F}$ (R12) and O_2+O_F recombination (R11), based on the observation by Janssen and Tuzson (2010) that wall assisted ozone formation is an essential part of oxygen plasma chemistry. Booth *et al* (2023), addressing the same material, concluded that the description of the experimental ozone behaviour in the afterglow requires considering surface production of O_3 from the reaction of O_2 molecules with adsorbed O atoms (R11). We should notice that $O_{2,F}+O_{2,F}$ reactions are neglected, since the fraction of $O_{2,F}$ is expected to be low, due to the lower desorption barrier for $O_{2,F}$ than for O_F. Finally, no recombination mechanisms are considered between O_2 and O_S, neither E-R O_2+O_S nor L-H $O_{2,F}+O_S$. This is due to the high energy barrier to break the chemisorption bond that turns this reaction thermodynamically unfavourable with a too low probability to have an influence in O recombination or O_3 production (Marinov 2012).

Besides the added reactions and rates, the upgraded model includes changes in parameters (table 6) with respect to the base model (table 4). Indeed, in table 6, the additional parameters and the modified parameters are signaled by different marks. Some parameters were changed to adjust the simulation results to the experimental data at $T_w = 5\,°C$ (see figure 4(a)). Following the analysis of figure 4, the influence of $O+O_S$ recombination at high T_{nw} is increased by slightly decreasing the recombination barrier of this process (E_{ER}^S) from 17.5 kJ $\cdot$ mol^{-1} to 15.0 kJ $\cdot$ mol^{-1}. In order to counteract the increase of the simulated γ_O, the barrier of O_F+O_S recombination (E_{LH}^S) is slightly increased from 17.5 kJ $\cdot$ mol^{-1} to 20.0 kJ $\cdot$ mol^{-1}, with effects mostly at low T_{nw}. Following the discussion of parameters by Guerra and Marinov (2016), these values are reasonable. They are within the intervals, or lie close to the values in literature of 15.8 kJ $\cdot$ mol^{-1} (Lopaev *et al* 2011a, 2011b), 17 kJ $\cdot$ mol^{-1} (Kim and Boudart 1991), 25 kJ $\cdot$ mol^{-1} (Kovalev *et al* 2005) and 25.5 kJ $\cdot$ mol^{-1} (Guerra 2007). Moreover, they remain close to the diffusion barrier E_D (15 kJ $\cdot$ mol^{-1}) (Lopaev *et al* 2011a). While in the base model $E_{LH}^S = E_{ER}^S$, this is no longer the case in the upgraded model where there is a 5 $\mathrm{kJ\cdot mol^{-1}}$ difference between them. It is reasonable to consider that an extra diffusion barrier of this relatively small magnitude may exist in the vicinity of a chemisorption site due to local structure modifications, as also considered by Afonso *et al* (2024) in the case of metastable chemisorption sites (in that case an extra barrier of 15 $\mathrm{kJ\cdot mol^{-1}}$ was taken). Apart from these small changes, the main change in the upgraded model concerns the parameter with largest uncertainty in literature, the pre-exponential factor of the desorption frequency ν_d (Guerra and Marinov 2016). By varying this parameter with wall temperature, an agreement between simulations and experiments is obtained for every case in both experimental data sets, as shown in section 4.1, without changing any of the other parameters in table 6 (most of them taken directly from table 4 of the base model).

The desorption frequency pre-exponential factor ν_d was discussed by Ibach *et al* (1980) for a well characterized system of CO interaction on Ni(111). It was noticed that transition-state theory predicts a linear dependence with T_w for ν_d for the desorption of a single atom out of a one dimensional potential: $\nu_\mathrm{d} = k_\mathrm{B}T_\mathrm{w}/h = 6\times10^{12}(\frac{T_\mathrm{w}}{300\ \mathrm{K}})\ \mathrm{s}^{-1}$ (Marschall and MacLean 2011). This justifies the usual choice of $\nu_\mathrm{d} = 10^{13}\ \mathrm{s}^{-1}$ (Lopaev *et al* 2011a, Booth *et al* 2019). However, by addressing the equilibrium between the gas phase and the adsorbed phase, Ibach *et al* (1980) found that ν_d should have values closer to $10^{15}\ \mathrm{s}^{-1}$, as used in the seminal work by Kim and Boudart (1991), rather than $10^{13}\ \mathrm{s}^{-1}$, and it should be dependent on T_w and adsorption site coverage. Booth *et al* (2023) also argued that taking into account collisions between gaseous particles and the surface can increase ν_d from $10^{13}\ \mathrm{s}^{-1}$ to $10^{15}\ \mathrm{s}^{-1}$. Ibach *et al* (1980) further presented experimental data demonstrating an exponential increase of ν_d with the coverage, which, in its turn, decreases with T_w. The same effect was reported with CO on Ru(001) surfaces (Pfnür *et al* 1978). According to Ibach *et al* (1980), such an increase of ν_d with coverage is indicative of repulsive interactions between the adsorbed species, that facilitate desorption or avoid adsorption.

In this work, we estimate ν_d by matching the simulation results with experimental data set 2 and then confirming the good agreement also with data set 1. We tried to correlate the estimated values of ν_d with the coverage of physisorption sites (which depend not only on T_w but also on discharge parameters), but no good fit or clear dependence of ν_d on coverage was found. Nevertheless, we find an exponential growth of the estimated ν_d with the median coverage for each T_w, in agreement with Ibach *et al* (1980), which can also be described as an exponential decay of ν_d with T_w. Indeed, the approximate values of ν_d that match experimental data set 2 are $2.0\times10^{15}\ \mathrm{s}^{-1}$ for $T_\mathrm{w} = -20\,^\circ\mathrm{C}$ (253.15 K), $9.0\times10^{14}\ \mathrm{s}^{-1}$ for $T_\mathrm{w} = 5\,^\circ\mathrm{C}$ (278.15 K), $4.5\times10^{14}\ \mathrm{s}^{-1}$ for $T_\mathrm{w} = 25\,^\circ\mathrm{C}$ (298.15 K) and $3.0\times10^{14}\ \mathrm{s}^{-1}$ for $T_\mathrm{w} = 50\,^\circ\mathrm{C}$ (323.15 K). These values are within the limits discussed by Guerra and Marinov (2016) ($10^{13}\ \mathrm{s}^{-1}$ and $10^{16}\ \mathrm{s}^{-1}$) and are perfectly fitted by the expression represented in figure 5:

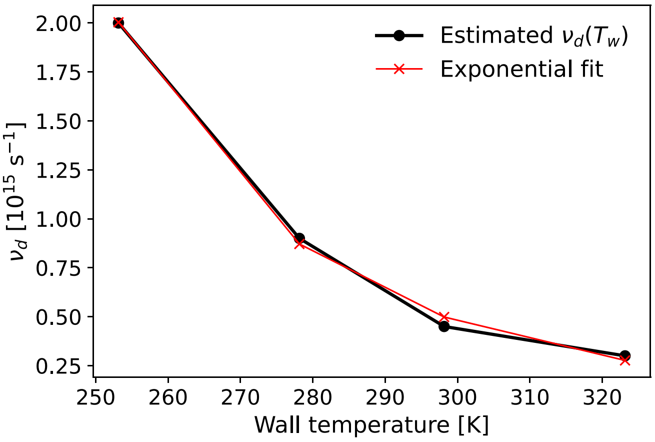

Figure 5. Desorption frequency as function of the wall temperature. ν_d estimated by matching simulation results of γ_O with the measurements of data set 2 for $T_\mathrm{w} = -20\ ^\circ\mathrm{C}, 5\ ^\circ\mathrm{C}, 25\ ^\circ\mathrm{C}, 50\ ^\circ\mathrm{C}$. The fit is given by equation (13).

$$\nu_\mathrm{d}\left(T_\mathrm{w}\right) = 10^{15}\times\left(0.01634 + 1.67\times10^{-4}\cdot\exp\left(\frac{19.75\ \mathrm{kJ\cdot mol^{-1}}}{R\,T_\mathrm{w}}\right)\right)s^{-1}. \tag{13}$$

In this way, by varying the most uncertain and temperature dependent parameter, ν_d, we find an effective way to account for more complex, multi-step kinetics phenomena absent from mesoscopic models. It should be noticed that it is experimentally difficult to distinguish differences in ν_d from differences in the desorption barrier energies E_d^O and $E_\mathrm{d}^{\mathrm{O}_2}$ and that the same effect could be obtained by varying E_d^O and $E_\mathrm{d}^{\mathrm{O}_2}$ with the wall temperature (or surface coverage), instead of changing ν_d. Indeed, by fitting experimental results, Tait *et al* (2006) proposed decreasing desorption barriers of alkanes/hydrocarbons on different surfaces with surface coverage, for small coverages, indicating the presence of adsorption sites with different adsorption energies. This would mean increasing desorption barriers with T_w, which is coherent with the results in this work. The variation of ν_d is preferred in this work with respect to a possible variation of E_d^O and $E_\mathrm{d}^{\mathrm{O}_2}$ because ν_d is more uncertain (Guerra and Marinov 2016). Further research is required to clarify this point.

To highlight the role of the different changes between the base and upgraded models, figure 6 shows the comparison with experimental data set 1 of the simulation results of the base model, the base model with $\nu_\mathrm{d}(T_\mathrm{w})$ and the upgraded model. The comparison demonstrates that the consideration of the wall temperature dependent pre-exponential factor of the desorption frequency is essential to bring the γ_O results to the appropriate values at each T_w, but the remaining changes and additions are still necessary to obtain an adequate evolution of γ_O with T_nw. The relevance of each recombination mechanism of the upgraded model and its influence on the shape of the $\gamma_\mathrm{O}(300/T_\mathrm{nw})$ curve is further shown and explained in section 4.2.

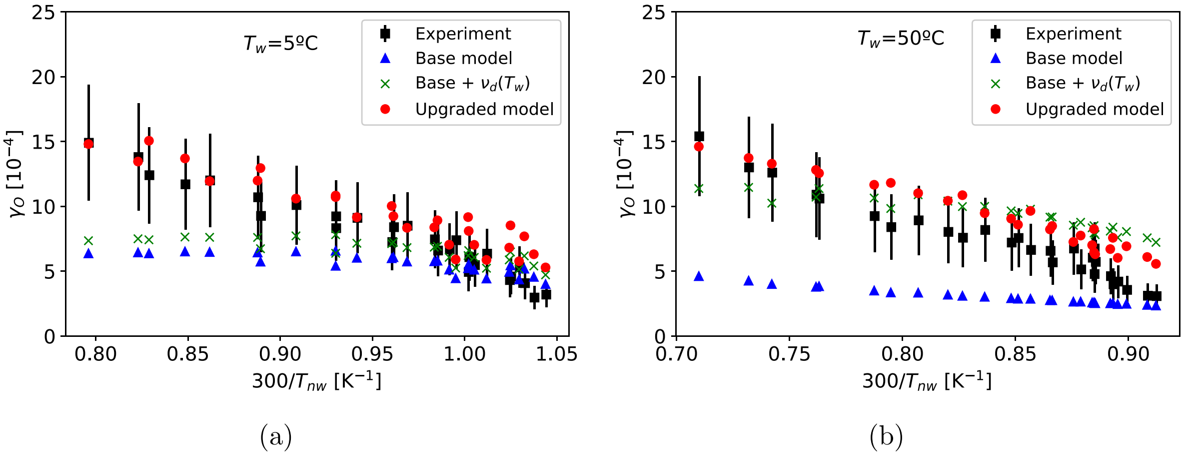

Figure 6. O atom wall loss probability in Pyrex as function of the reverse of the near-wall temperature, for (a) $T_w = 5\,°C$ and (b) $T_w = 50\,°C$. Results from experimental measurements from data set 1 (Booth *et al* 2019) and from simulations employing the base model, the base model with modified $\nu_d(T_w)$ and the upgraded model.

4. Results

4.1. Validation of the upgraded model against experimental results

The results of all the models presented in the previous section were already compared to experimental data set 1 in figures 3, 4 and 6. Figure 7 shows the recombination probability γ_O as function of the reverse of T_{nw} for the conditions of data set 2. The experimental results are compared to the calculations of the analytical model by Booth *et al* (2019), already shown to provide the same results as the corresponding numerical model, to the simulations of the base model and to those of the upgraded model, all described in section 3.

Figure 7 shows that the simulation results employing the upgraded model match very well, mostly within the ±30% error bars, the measurements of data set 2. This may not look too surprising since the pre-exponential factor of the desorption frequency $\nu_d(T_w)$ is chosen for each T_w to match these measurements. Nevertheless, the results show a remarkable consistency of the model for a significant range of T_{nw} (corresponding to different conditions of current and pressure) and of T_w, just by assuming a smooth T_w dependency of a single parameter, $\nu_d(T_w)$, with all the other parameters remaining based on literature and close to the base reaction set. The consistency and agreement with experiments is also maintained when changing the experimental conditions, in this case from those of data set 1 (figure 6) to those of data set 2. For both data sets, it is shown that the base model presents a worse agreement with experiments than the upgraded model, calculating too high loss probability γ_O at low T_w and too low γ_O at high T_w. Also the dependency of γ_O from T_{nw} is more accurately described by the upgraded model than the base model, as it is visible that the steepness of the decrease of γ_O with $300/T_{nw}$ is generally higher in experiments than in the base model simulations.

Finally, figure 7 shows that the model by Booth *et al* (2019) presents a good agreement with the measurements of data set 2 for $T_w = 5\,°C$ and for $T_w = 50\,°C$, as in the case of data set 1. Moreover, the agreement within the errorbars is confirmed for $T_w = 25\,°C$, the case in between the previous two wall temperatures. Nevertheless, the model by Booth *et al* (2019) overestimates γ_O for $T_w = -20\,°C$, which points to a limitation of the model, which has only two recombination reactions and no T_w dependence in any parameter, to being extended to varying conditions.

4.2. Recombination mechanisms

The validated upgraded model is then used to analyse through which mechanisms is atomic oxygen recombined back into molecular form in the Pyrex wall for different conditions. This is done by assessing the contributions of the different recombination reactions in table 5 to the calculation of the recombination probability γ_O. The comparison of the different contributions is shown firstly for the conditions of data set 1 in figure 8. Besides the total γ_O from experiments and simulations, the main contributions to γ_O for each wall temperature case are displayed. These are the 4 most relevant recombination mechanisms in each case among the 5 following processes: E-R with $O + O_S$ (R4), E-R with $O + O_F$ (R5), L-H with $O_F + O_S$ (R7), L-H with $O_F + O_F$ (R8) and E-R with $O_2 + O_F$ (R11). From the O recombination processes of table 5 (R4, R5, R7, R8, R11, R13, R14 and R15), we should notice that R13-15 are negligible due to the $O_{2,F}$ fraction of physisorption sites (between 2×10^{-7} and 3×10^{-6}) being one to two orders of magnitude lower than the O_F fraction (between 8×10^{-6} and 4×10^{-5}), according to the upgraded model in the conditions of data set 1. This takes place in spite of O_2 having between 4 and 27 times higher number density in the plasma than O, mostly due to the higher surface desorption barrier considered for O ($30\ \mathrm{kJ \cdot mol^{-1}}$) than for O_2 ($17.5\ \mathrm{kJ \cdot mol^{-1}}$), which is determinant for the loss of physisorbed species. As a result, R11 is the dominant reaction for O_3 wall production, as pointed out by Booth *et al* (2023).

Figure 8(a) shows that for low wall temperature, $T_w = 5\,°C$, the main recombination mechanisms according to the model

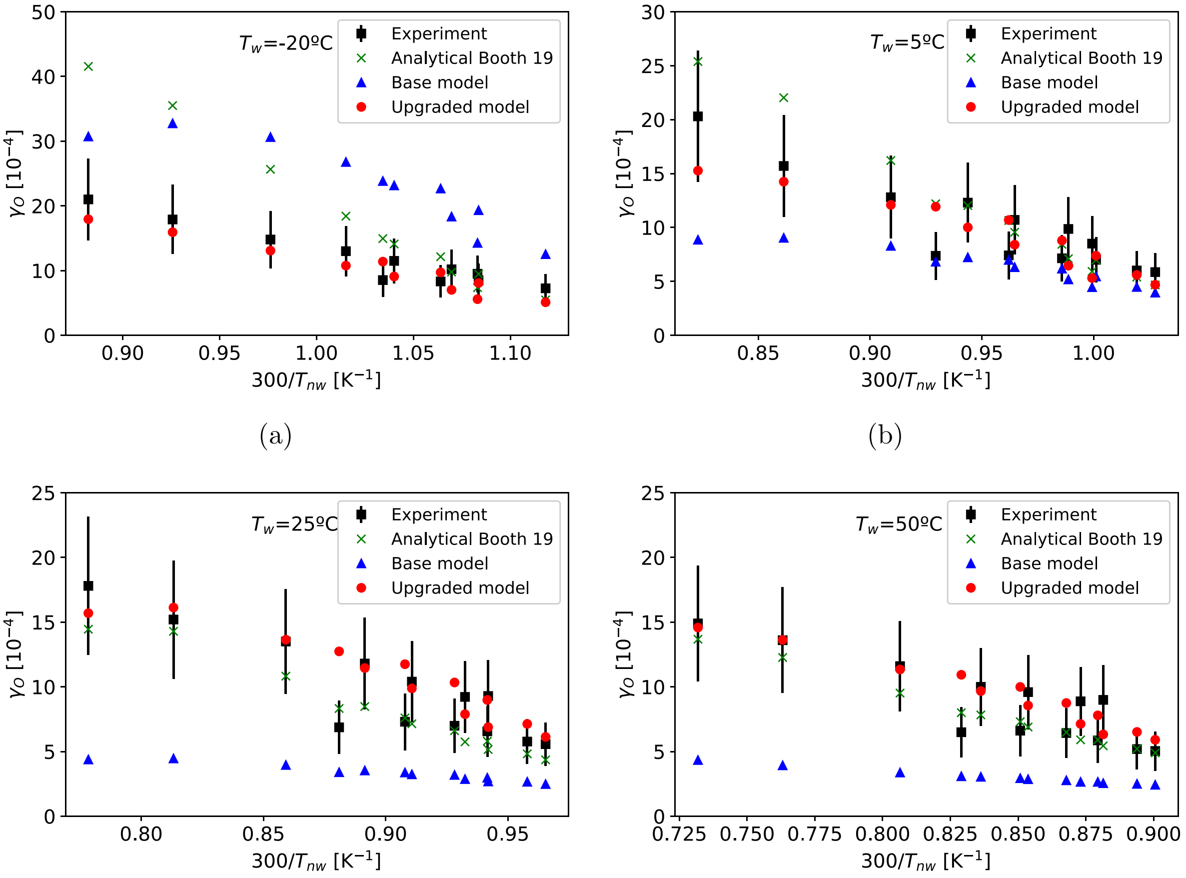

(a) (b)

(c) (d)

Figure 7. O atom wall loss probability in Pyrex as function of the reverse of the near-wall temperature, for (a) $T_w = -20\,^\circ$C, (b) $T_w = 5\,^\circ$C, (c) $T_w = 25\,^\circ$C and (d) $T_w = 50\,^\circ$C. Results from experimental measurements from data set 2 and from the three different models presented in section 3.

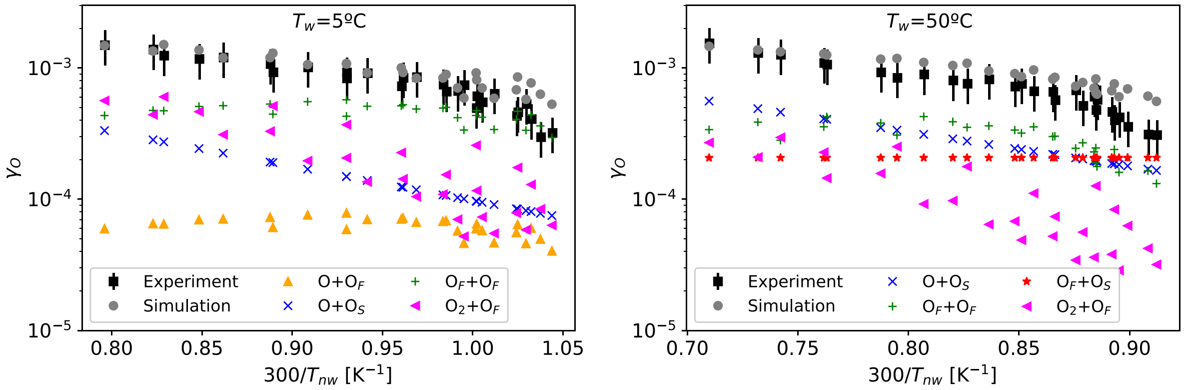

(a) (b)

Figure 8. O atom wall loss probability in Pyrex as function of the reverse of the near-wall temperature, for (a) $T_w = 5\,^\circ$C and (b) $T_w = 50\,^\circ$C. Results from experimental measurements from data set 1 (Booth *et al* 2019) and from simulations employing the upgraded model. The simulation results presented include the total γ_O (●) and the contributions of the 4 most relevant recombination mechanisms.

are L-H with $O_F + O_F$ (R8) and E-R with $O_2 + O_F$ (R11), which are also the main processes inducing the curvature in the results, represented as $\log(\gamma_O)$ $vs 300/T_{nw}$. The curvature is the result of the O_F fraction tendentiously increasing with T_{nw} while the particle fluxes from the gas phase have a complex dependency of T_{nw} (whose rise increases the thermal velocity), pressure and current, since the dissociation degree tends to decrease with pressure and increase with current, within

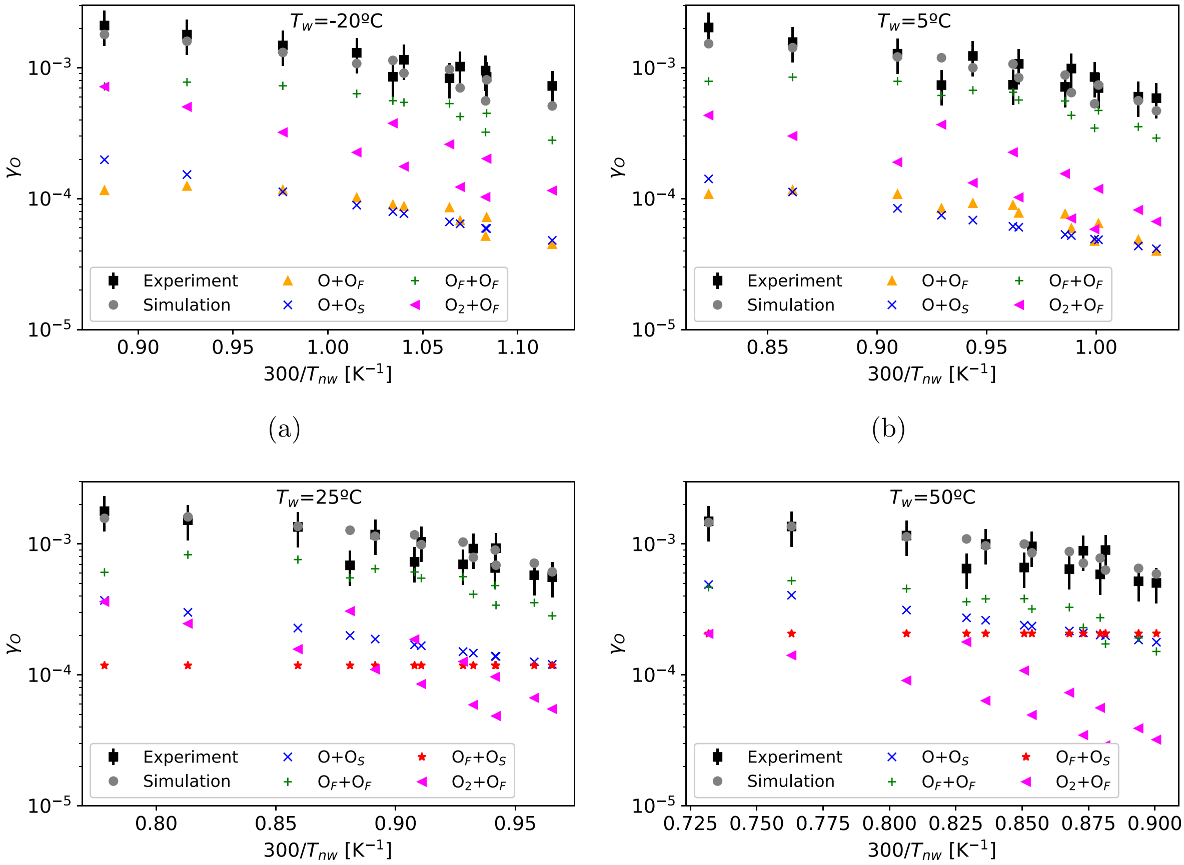

(a) (b)

(c) (d)

Figure 9. O atom wall loss probability in Pyrex as function of the reverse of the near-wall temperature, for (a) $T_w = -20\,°C$, (b) $T_w = 5\,°C$, (c) $T_w = 25\,°C$ and (d) $T_w = 50\,°C$. Results from experimental measurements from data set 2 and from simulations employing the upgraded model. The simulation results presented include the total γ_O (●) and the contributions of the 4 most relevant recombination mechanisms.

the studied range (Booth *et al* 2019). For higher wall temperature, $T_w = 50\,°C$, figure 8(b) shows that E-R with $O + O_S$ (R4) and L-H with $O_F + O_S$ (R7) can be as or more important than E-R with $O_2 + O_F$ (R11) and L-H with $O_F + O_F$ (R8). It should be noticed that the contribution of E-R with $O + O_S$ (R4) depends only on T_{nw}, which increases with T_w, with that process becoming relevant for high values of T_{nw}, in agreement with literature (Macko *et al* 2004, Guerra 2007). The remaining contributions do not present such a sharp increase with T_{nw} due to not having a T_{nw} dependent rate or not depending on an increasing flux of atomic oxygen with T_{nw}. As a result, they become less relevant with increasing T_{nw}, when compared to E-R with $O + O_S$ (R4). Moreover, the contribution of L-H recombination with $O_F + O_S$ (R7) increases with T_w, following the dependence of the recombination rate. In the opposite direction, the relevance of E-R with $O_2 + O_F$ (R11), of E-R with $O + O_F$ (R5) and of L-H with $O_F + O_F$ (R8) decreases with T_w due to the higher desorption rate of physisorbed atoms.

The analysis of the contributions of the different recombination mechanisms is continued in figure 9, where the same comparisons are presented as in figure 8 but for data set 2, thus extending the wall temperature range of the analysis. The previous assessment is coherent for the different conditions of data set 2. We can conclude from the figures that, according to the model presented in this work and in the studied conditions, L-H with $O_F + O_F$ (R8) and E-R with $O_2 + O_F$ (R11) are the dominant oxygen recombination mechanisms for $T_w = -20\,°C$ and $T_w = 5\,°C$, while for $T_w = 25\,°C$ and $T_w = 50\,°C$ the contributions of E-R with $O + O_S$ (R4) and L-H with $O_F + O_S$ (R7) also play a relevant role.

The dependence of the different contributions to recombination on T_w is further shown in figure 10, where γ_O simulated with the upgraded model in some conditions of data set 2 is presented as function of T_w, along with the contributions of the five major recombination mechanisms. Two cases of discharge current (20 mA and 40 mA) and pressure (0.8 Torr and 3 Torr) are considered, in a total of 4 subfigures. To assist the interpretation of the results, figure 11 presents the surface site coverages for the same conditions. The surface fraction of O_S is not shown because it always occupies close to 100% of the chemisorption sites, i.e. a 1.5×10^{-2} fraction of the total number of sites. It is clearly visible from figure 10 that the contributions of E-R with $O + O_S$ (R4) and L-H with $O_F + O_S$ (R7) increase with T_w, in the first case due to the increasing flux and in the second case due to the increasing rate. They are thus expected to be the dominant recombination mechanisms

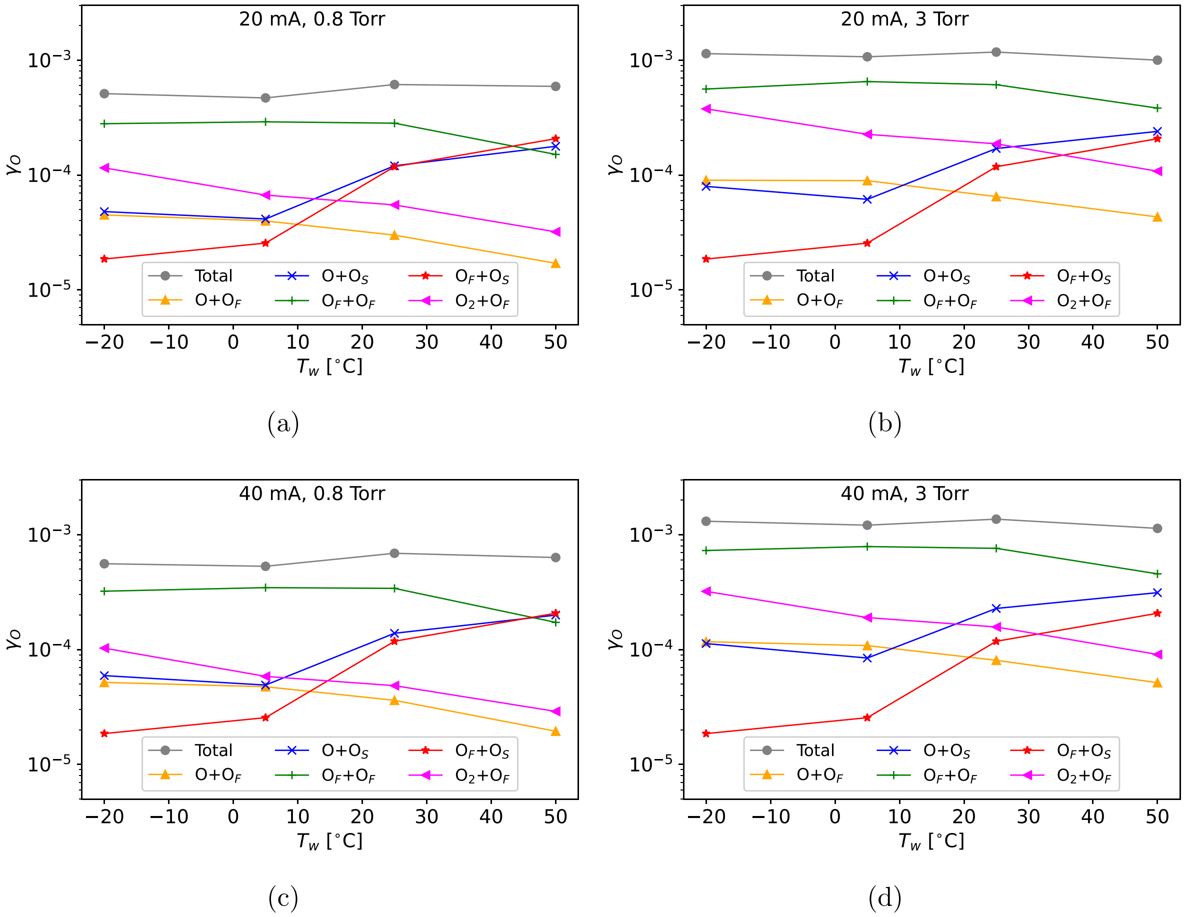

(a) (b)

(c) (d)

Figure 10. O atom wall loss probability in Pyrex as function of the wall temperature for the conditions of data set 2, for (a) $I = 20$ mA and $p = 0.8$ Torr, (b) $I = 20$ mA and $p = 3$ Torr, (c) $I = 40$ mA and $p = 0.8$ Torr and (d) $I = 40$ mA and $p = 3$ Torr. Results from simulations employing the upgraded model. The simulation results presented include the total γ_O (●) and the contributions of the 5 most relevant recombination mechanisms.

for T_w higher than 50 °C and, in the case of $O + O_S$, to keep increasing with T_w (Guerra and Marinov 2016). The contributions of the mechanisms involving O_F and not O_S ($O + O_F$, $O_2 + O_F$ and $O_F + O_F$) decrease with T_w due to the decreasing fraction of O_F, shown in figure 11. These mechanisms are expected to keep being dominant for T_w lower than −20 °C. It is also noticeable in figure 10 that increasing pressure generally induces higher recombination probabilities, in agreement with the higher coverage of O_F presented in figure 11. The flux of O_2 responsible for the $O_2 + O_F$ recombination producing ozone also increases with pressure. The dependence on current is less clear in figure 10, although there is also a general increase of γ_O with current. One aspect that can be noticed when increasing current from 20 mA to 40 mA is that the contribution from $O + O_F$ approaches that of $O_2 + O_F$, due to the increasing dissociation degree in the plasma.

4.3. Discussion on recombination mechanisms and ozone production

The measured and simulated γ_O are within the expected range for Pyrex for the studied conditions, between 10^{-4} and 10^{-2} (Pagnon *et al* 1995, Gordiets and Ferreira 1998, Macko *et al* 2004). In the work by Macko *et al* (2004), where γ_O was measured in Pyrex in the afterglow, E-R mechanisms appear to be dominant for wall temperatures above 250 K ($\simeq -20$ °C), due to a linear evolution of $\log(\gamma_O)$ vs $1000/T_w$, without distinction between T_w and T_{nw}. These results were described by calculations by Guerra (2007). In this work, we find almost linear dependences of $\log(\gamma_O)$ with $300/T_{nw}$ for wall temperatures between 253 K and 323 K, while having both E-R and L-H mechanisms being significant for recombination, which may not be contradictory with the results by Macko *et al* (2004). In fact, L-H was suggested to be dominant or as important as E-R for O recombination on silica-like materials in the range of T_w between 250 K and 500 K in the works by Kim and Boudart (1991), Gordiets *et al* (1996), Gordiets and Ferreira (1998), Cacciatore *et al* (1999), Guerra and Marinov (2016), Marinov *et al* (2017), Guerra *et al* (2019). Those studies assume E-R recombination to take place between O and O_S. In this work the picture is more complex, with E-R mechanisms O_2+O_F and O+O_F being as significant or even more than O+O_S for T_w up to 298.15 K (25 °C). Within this description, the linear dependence of $\log(\gamma_O)$ with $300/T_{nw}$ can be obtained from both E-R and L-H mechanisms, while L-H with O_F+O_F is shown to be fundamental to obtain a curvature at low T_{nw}.

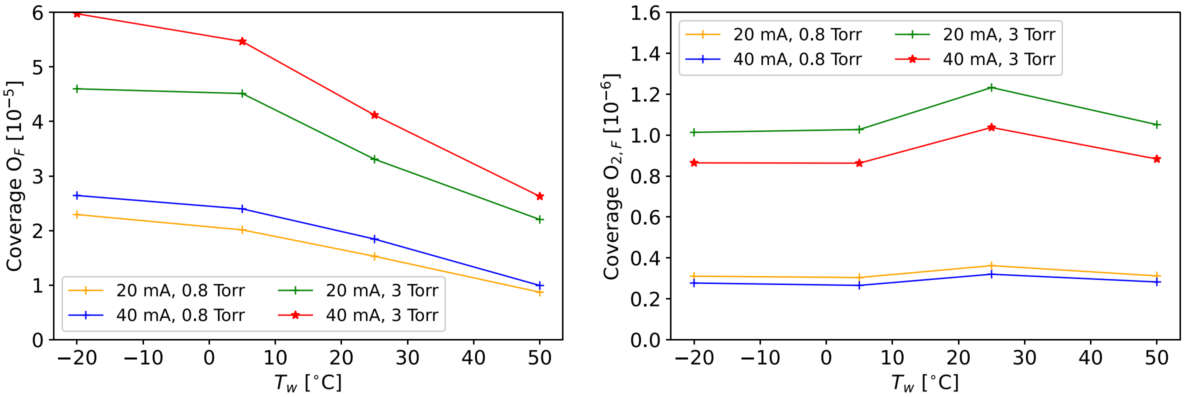

(a) (b)

Figure 11. Fractions of physisorption site occupation as function of the wall temperature for the conditions of data set 2 and figure 10. Occupation by (a) O_F and (b) $O_{2,F}$. Results from simulations employing the upgraded model.

We should add that $O+O_F$ is not a dominant recombination mechanism in the upgraded model, being consistently less significant than O_2+O_F and O_F+O_F recombination mechanisms. This is not the case employing the reaction set by Booth *et al* (2019), where the desorption frequency is low and $O+O_F$ may be an effective way to consider other recombination mechanisms involving O_F. Indeed, employing the upgraded model, the estimated average number of hops of a physisorbed atom during its lifetime on the surface (calculated as in equation (10) in the paper by Marinov *et al* (2017)) lies between 6 and 10 in the conditions under study. This means that long distance diffusion of O_F may not have an important role and thus the differences between considering an effective $O+O_F$ recombination mechanism and a more detailed scheme may be more conceptual than practical.

The surface kinetics simulations results should also be discussed in terms of coherence with the knowledge of the plasma under study, namely in what concerns ozone wall production (via R11 and R13-15). Janssen and Tuzson (2010) studied the isotopic compositions of ozone in an oxygen discharge in Pyrex at pressures between 1.75 and 12.5 Torr and concluded that the atom recombination coefficient into ozone $\gamma_{O\rightarrow O_3}$ should be of the order of 4×10^{-3} at room temperature and slightly higher at lower temperatures. This value was considered in the recent work by Meyer *et al* (2023). The model results by Lopaev *et al* (2011a, 2011b) also reported $\gamma_{O\rightarrow O_3}$ in an oxygen glow discharge in quartz increasing almost linearly with pressure between 5 and 50 Torr up to 6×10^{-3} (approximately 5×10^{-4} at 5 Torr and 10^{-3} at 10 Torr), via the $O+O_{2,F}$ (R13) and O_2+O_F (R11) processes. The analysis of measurements by Marinov *et al* (2013a) in oxygen post-discharge after short pulses found that at room temperature and 5 Torr, ozone production should account for approximately 25% of the oxygen atom loss rate on the surface of non-treated silica fibres. Nevertheless, the combined experimental and modelling study by Marinov *et al* (2013b) on the same pulse post-discharge in the pressure range of 1-5 Torr for discharge currents between 40 and 120 mA concluded that ozone formation at the wall does not contribute significantly to the total ozone production. In that work, the total γ_O was assumed to be 2×10^{-4}, lower in post-discharge than under direct plasma exposure, as is typically the case in literature. Upper limits were suggested by Marinov *et al* (2013b) for $\gamma_{O\rightarrow O_3}$ as 10^{-5} at 1 Torr and 10^{-4} (half of γ_O) at 5 Torr. Simulations of similar post-discharge conditions by Guerra *et al* (2019) found slightly lower $\gamma_{O\rightarrow O_3}$, within the upper limits presented by Marinov *et al* (2013b). Under conditions similar to those of this work, for 40 mA, 20 °C wall temperature and pressures between 0.5 and 4 Torr, Booth *et al* (2023) reported simulation results in the early afterglow of O_3 surface production fluxes of $2\times10^{18}-1.5\times10^{19}\mathrm{m}^{-2}\cdot\mathrm{s}^{-1}$ and O fluxes to the wall of the order of $1-5\times10^{22}\mathrm{m}^{-2}\cdot\mathrm{s}^{-1}$, which results in $\gamma_{O\rightarrow O_3}$ of the order of 10^{-4}. The simulation results of $\gamma_{O\rightarrow O_3}$ presented in this work clearly increase with pressure and O_2 density, as in the literature, and they decrease with current and T_w, due to dissociation and desorption, respectively. They have values between 10^{-5} and 10^{-3}, within the ranges found in the discharge studies by Janssen and Tuzson (2010) and by Lopaev *et al* (2011a, 2011b) and in the post-discharge study by Booth *et al* (2023), but above the upper limit of 10^{-4} indicated for post-discharge by Marinov *et al* (2013b).

Another way to verify O_3 wall production is to assess its self-consistency with simulation results of O_3 volume losses. This will be done more consistently in the near future by coupling the surface model to the global model presented by Dias *et al* (2023). However, a first verification can be done here that the ozone surface production rate, obtained mostly via reaction R11 but also through R13-15, is consistent with the expected ozone loss rate in the plasma. The ozone production rate can be calculated as $S_{O_3}=[O]_{av}\times\nu_{O\rightarrow O_3}=[O]_{av}\times\gamma_{O\rightarrow O_3}\frac{v_{O,th}}{2R_{tube}}$, where $\gamma_{O\rightarrow O_3}=\gamma_{11}+\gamma_{13}+\gamma_{14}+\gamma_{15}$, $v_{O,th}$ is the atomic oxygen thermal velocity at temperature T_{nw} and R_{tube} is the reactor tube inner radius of 1 cm. For data set 1, for $T_w=50\,°\mathrm{C}$, $\nu_{O\rightarrow O_3}$ lies between 1 s^{-1} and 13 s^{-1}, within the range of O loss frequency measured by Booth *et al* (2019). Therefore, S_{O_3} is limited between 3×10^{21} $\mathrm{m}^{-3}\cdot\mathrm{s}^{-1}$ (low pressure 0.75 Torr) and 9×10^{22} $\mathrm{m}^{-3}\cdot\mathrm{s}^{-1}$ (high pressure 10 Torr). In the simulation results of the zero-dimensional chemical kinetics model by

Viegas *et al* (2023) (without O_3 surface production or loss) in the conditions of that work, addressing the same discharge as in this work for 30 mA discharge current and $T_w = 50\,°C$, the calculated total loss rate of O_3 is 1.2×10^{21} $m^{-3} \cdot s^{-1}$ at 0.75 Torr and 8.5×10^{22} $m^{-3} \cdot s^{-1}$ at 10 Torr, slightly lower than the production rate in this work. However, in the work by Viegas *et al* (2023) the O_3 density from zero-dimensional results is shown to be underestimated with respect to the O_3 density from 1D results by up to a factor 3. A higher O_3 density would of course result in a higher loss rate, coherent with the production rate in this work. As such, the O_3 production rate found in this work is reasonable and the associated mechanism (R11) may be a valuable complement to the reaction set by Dias *et al* (2023).

5. Conclusions

This work addresses surface kinetics in an oxygen DC glow discharge in a Pyrex (borosilicate glass) tube with 1 cm inner radius at intermediate pressure. Oxygen surface recombination is studied via mesoscopic modelling and comparison with experiments. Two experimental sets of conditions and of measured data are assessed: one previously published and a new one. They compose a total of 106 experimental conditions with discharge current varying between 10 and 40 mA, pressure values ranging between 0.75 and 10 Torr, and fixed outer wall temperatures (T_w) of $-20\,°C$, $5\,°C$, $25\,°C$ and $50\,°C$. The lower pressure conditions addressed recently by Afonso *et al* (2024), in which work ion-induced reversible surface modification was put forward, are left out of this study.

Three reaction sets for mesoscopic surface modelling are presented and compared: one based on the work by Booth *et al* (2019), one by Marinov *et al* (2017) and an upgraded reaction set developed in this work. It is shown that the analytical model by Booth *et al* (2019) can be reproduced numerically and its results of recombination probability (γ_O) agree well with measurements at $T_w = 5, 25$ and $50\,°C$ but overestimate measurements at $T_w = -20\,°C$. The model developed in this work is based on the mesoscopic model by Marinov *et al* (2017) but adds further reactions to it and is inspired by the parametric studies by Morillo-Candás (2019) and Silveira (2023). The upgraded model considers the pre-exponential factor of the O and O_2 desorption frequency as being exponentially dependent on the inverse of the wall temperature. This is based on insights by Ibach *et al* (1980) and attributed to repulsive interactions between adsorbed species, whose population decreases with wall temperature. After these upgrades, the model is validated by a remarkable agreement of γ_O with experiments for the 106 studied conditions of wall temperature, pressure, current and near-wall temperature. This validation effort is a great display of versatility and of the expected predictability when changing conditions. It provides confidence in results and allows to use the model to deepen the knowledge in such complex reaction kinetics. Despite the good results and the indications that the pre-exponential factor of the desorption frequency may depend on the wall temperature, this consideration may as well be an effective way of capturing more complex kinetics, such as multi-step processes, varying adsorption and desorption energy barriers and varying distributions of reactivity of surface sites. The chosen formulation of the upgraded model allows to provide a more complete description of the plasma-surface interactions, while keeping the simplicity of a mesoscopic model.

The analysis of the upgraded model results highlights that L-H recombination with $O_F + O_F$ and E-R recombination with $O_2 + O_F$ are the dominant oxygen recombination mechanisms in Pyrex for $T_w = -20\,°C$ and $T_w = 5\,°C$. For $T_w = 25\,°C$ and $T_w = 50\,°C$ the contributions of E-R with $O + O_S$ and L-H with $O_F + O_S$ also play a relevant role for O surface recombination. As such, the more complex picture introduced in this work allows to describe experimental results of O recombination probability through a combination of both E-R and L-H mechanisms with different reactants. Finally, the ozone wall production rate predicted in this work for Pyrex is considered reasonable and is shown to be relevant not only for O recombination but also for the global ozone production rate in plasmas in the studied conditions. The ozone wall production rate clearly increases with pressure, with relevance also for higher pressure discharge regimes. In the future, we intend to couple the surface kinetics model to a plasma global model and extend it to other pressure regimes and gas mixtures.

The same formalism developed in this work can be used to study recombination for other surfaces and atoms, both using a deterministic method as presented here or a Kinetic Monte Carlo model. However, each case has its one specificities, that needs to be taken into account. First, the appropriate surface parameters (active surface site density, adsorption energies, diffusion barriers and frequencies, etc) have to be considered, depending as well on the metallic or dielectric nature of the surface. Obtaining these parameters cannot be achieved solely within a mesoscopic model and requires fundamental experimental studies, such as the ones reported in this work, and/or the support from *ab initio* calculations (Marinov *et al* 2017). An assessment of the need to consider different elementary processes is also required. For instance, physisorption on top of chemisorption sites, dissociative chemisorption (Nave *et al* 2014, Kroes 2021), abstraction (Sholl 1997, Khanom *et al* 2003) or a distribution of reactivity among the adsorption sites (Donnelly *et al* 2011, Marinov 2019) may have to be included. Nevertheless, once the relevant mechanisms have been identified, the extension of the current model to describe any of them is straightforward.

Data availability statement

All data that support the findings of this study are included within the article (and any supplementary files).

Acknowledgments

IPFN activities were supported by the Portuguese FCT—Fundação para a Ciência e Tecnologia, I.P., by project reference UIDB/50010/2020 (https://doi.org/10.54499/UIDB/50010/2020), by project reference UIDP/50010/2020 (https://doi.org/10.54499/UIDP/50010/2020) and by project reference LA/P/0061/2020 (https://doi.org/10.54499/LA/P/0061/2020). This work was further supported by FCT under projects PD/BD/150414/2019 (PD-F APPLAuSE) and PTDC/FIS-PLA/1616/2021 (PARADiSE, https://doi.org/10.54499/PTDC/FIS-PLA/1616/2021). PV acknowledges support by project CEECIND/00025/2022 of FCT. ASMC acknowledges funding by LabEx Plas@par receiving financial aid from the French National Research Agency (ANR) under project SYCAMORE, reference ANR-16-CE06-0005-01. The authors acknowledge the useful insights provided by italian CNR and ISTP researcher Dr Maria Rutigliano, by Professor Leon Lefferts of the University of Twente and Drs. Dmitry Lopaev and Dmitry Voloshin of Moscow State University.

ORCID iDs

Pedro Viegas https://orcid.org/0000-0002-3820-3300
Tiago Cunha Dias https://orcid.org/0000-0002-2179-1345
Olivier Guaitella https://orcid.org/0000-0002-6509-6934
Ana Sofía Morillo Candás https://orcid.org/0000-0002-6974-1240
Vasco Guerra https://orcid.org/0000-0002-6878-6850

References

Afonso J, Vialetto L, Guerra V and Viegas P 2024 Plasma-induced reversible surface modification and its impact on oxygen heterogeneous recombination *J. Phys. D: Appl. Phys.* **57** 04LT01

Alves L L, Bogaerts A, Guerra V and Turner M M 2018 Foundations of modelling of nonequilibrium low-temperature plasmas *Plasma Sources Sci. Technol.* **27** 023002

Annusová A, Marinov D, Booth J P, Sirse N, da Silva M L, Lopez B and Guerra V 2018 Kinetics of highly vibrationally excited $O_2(X)$ molecules in inductively-coupled oxygen plasmas *Plasma Sources Sci. Technol.* **27** 045006

Balat-Pichelin M, Badie J M, Berjoan R and Boubert P 2003 Recombination coefficient of atomic oxygen on ceramic materials under earth re-entry conditions by optical emission spectroscopy *Chem. Phys.* **291** 181–94

Bogaerts A, Neyts E C, Guaitella O and Murphy A B 2022 Foundations of plasma catalysis for environmental applications *Plasma Sources Sci. Technol.* **31** 053002

Booth J P *et al* 2022 Quenching of $O_2(b^1\Sigma_g^+)$ by $O(^3P)$ atoms. Effect of gas temperature *Plasma Sources Sci. Technol.* **31** 065012

Booth J P, Guaitella O, Chatterjee A, Drag C, Guerra V, Lopaev D, Zyryanov S, Rakhimova T, Voloshin D and Mankelevich Y 2019 Oxygen (^{3}P) atom recombination on a pyrex surface in an O_2 plasma *Plasma Sources Sci. Technol.* **28** 055005

Booth J P, Guaitella O, Zhang S, Lopaev D, Zyryanov S, Rakhimova T, Voloshin D, Chukalovsky A, Volynets A and Mankelevich Y 2023 Oxygen atom and ozone kinetics in the afterglow of a pulse-modulated DC discharge in pure O_2: an experimental and modelling study of surface mechanisms and ozone vibrational kinetics *Plasma Sources Sci. Technol.* **32** 095016

Booth J-P *et al* 2020 Determination of absolute $O(^3P)$ and $O_2(a^1\Delta_g)$ densities and kinetics in fully modulated O_2 dc glow discharges from the $O_2(X^3\Sigma_g^-)$ afterglow recovery dynamics *Plasma Sources Sci. Technol.* **29** 115009

Bourdon A and Bultel A 2008 Numerical simulation of stagnation line nonequilibrium airflows for reentry applications *J. Thermophys. Heat Transfer* **22** 168–77

Cacciatore M and Rutigliano M 2009 Dynamics of plasma-surface processes: E-R and L-H atom recombination reactions *Plasma Sources Sci. Technol.* **18** 023002

Cacciatore M, Rutigliano M and Billing G D 1999 Eley-Rideal and Langmuir-Hinshelwood recombination coefficients for oxygen on silica surfaces *J. Thermophys. Heat Transfer* **13** 195–203

Cartry G, Duten X and Rousseau A 2006 Atomic oxygen surface loss probability on silica in microwave plasmas studied by a pulsed induced fluorescence technique *Plasma Sources Sci. Technol.* **15** 479

Cartry G, Magne L and Cernogora G 1999 Atomic oxygen recombination on fused silica: experimental evidence of the surface state influence *J. Phys. D: Appl. Phys.* **32** L53

Cartry G, Magne L and Cernogora G 2000 Atomic oxygen recombination on fused silica: modelling and comparison to low-temperature experiments (300 K) *J. Phys. D: Appl. Phys.* **33** 1303

Chen G, Buck F, Kistner I, Widenmeyer M, Schiestel T, Schulz A, Walker M and Weidenkaff A 2020 A novel plasma-assisted hollow fiber membrane concept for efficiently separating oxygen from CO in a CO_2 plasma *Chem. Eng. J.* **392** 123699

Dias T C 2019 Atomic oxygen kinetics in CO_2 plasmas *MSc. Thesis* Instituto Superior Técnico - Universidade de Lisboa Portugal

Dias T C, Fromentin C, Alves L L, del Caz A T, Silva T and Guerra V 2023 A reaction mechanism for oxygen plasmas *Plasma Sources Sci. Technol.* **32** 084003

Donnelly V M, Guha J and Stafford L 2011 Critical review: plasma-surface reactions and the spinning wall method *J. Vac. Sci. Technol.* A **29** 010801

Gordiets B F and Ferreira C M 1998 Self-consistent modeling of volume and surface processes in air plasma *AIAA J.* **36** 1643–51

Gordiets B, Ferreira C M, Nahorny J, Pagnon D, Touzeau M and Vialle M 1996 Surface kinetics of N and O atoms in N_2-O_2 discharges *J. Phys. D: Appl. Phys.* **29** 1021

Gousset G, Panafieu P, Touzeau M and Vialle M 1987 Experimental study of a d.c. oxygen glow discharge by V.U.V. absorption spectroscopy *Plasma Chem. Plasma Process.* **7** 409–27

Graves D B and Brault P 2009 Molecular dynamics for low temperature plasma-surface interaction studies *J. Phys. D: Appl. Phys.* **42** 194011

Guerra V 2007 Analytical model of heterogeneous atomic recombination on silicalike surfaces *IEEE Trans. Plasma Sci.* **35** 1397–412

Guerra V, del Caz A T, Pintassilgo C D and Alves L L 2019 Modelling N_2-O_2 plasmas: volume and surface kinetics *Plasma Sources Sci. Technol.* **28** 073001

Guerra V and Loureiro J 2004 Dynamical Monte Carlo simulation of surface atomic recombination *Plasma Sources Sci. Technol.* **13** 85–94

Guerra V and Marinov D 2016 Dynamical Monte Carlo methods for plasma-surface reactions *Plasma Sources Sci. Technol.* **25** 045001

Ibach H, Erley W and Wagner H 1980 The preexponential factor in desorption - CO on Ni(111 *Surf. Sci.* **92** 29–42

Janssen C and Tuzson B 2010 Isotope evidence for ozone formation on surfaces *J. Phys. Chem.* A **114** 9709–19

Kersten H, Deutsch H, Steffen H, Kroesen G M W and Hippler R 2001 The energy balance at substrate surfaces during plasma processing *Vacuum* **63** 385–431

Khanom F, Aoki A, Rahman F and Namiki A 2003 D abstraction by H on Si(111) surfaces *Surf. Sci.* **536** 191–205

Kim Y C and Boudart M 1991 Recombination of oxygen, nitrogen and hydrogen atoms on silica: kinetics and mechanism *Langmuir* **7** 2999–3005

Kovalev V, Afonina N and Gromov V 2005 Heat transfer modelling to catalytic protection systems of space vehicles entering into Martian atmosphere *Proc. 24th Int. Symp. on Shock Waves* pp 597–602

Kovalev V and Kolesnikov A 2005 Experimental and theoretical simulation of heterogeneous catalysis in aerothermochemistry (a review) *Fluid Dyn.* **40** 669–93

Kristof J, Macko P and Veis P 2012 Surface loss probability of atomic oxygen *Vacuum* **86** 614–9

Kroes G-J 2021 Computational approaches to dissociative chemisorption on metals: towards chemical accuracy *Phys. Chem. Chem. Phys.* **23** 8962–9048

Kushner M J 2009 Hybrid modelling of low temperature plasmas for fundamental investigations and equipment design *J. Phys. D: Appl. Phys.* **42** 194013

Lopaev D V, Malykhin E M and Zyryanov S M 2011a Surface recombination of oxygen atoms in O_2 plasma at increased pressure: I. The recombination probability and phenomenological model of surface processes *J. Phys. D: Appl. Phys.* **44** 015201

Lopaev D V, Malykhin E M and Zyryanov S M 2011b Surface recombination of oxygen atoms in O_2 plasma at increased pressure: II. Vibrational temperature and surface production of ozone *J. Phys. D: Appl. Phys.* **44** 015202

Macko P, Veis P and Cernogora G 2004 Study of oxygen atom recombination on a Pyrex surface at different wall temperatures by means of time-resolved actinometry in a double pulse discharge technique *Plasma Sources Sci. Technol.* **13** 251

Marinov D 2012 Reactive adsorption of molecules and radicals on surfaces under plasma exposure *PhD Thesis* École Polytechnique France

Marinov D 2019 Kinetic Monte Carlo simulations of plasma-surface reactions on heterogeneous surfaces *Front. Chem. Sci. Eng.* **13** 815–22

Marinov D, Guaitella O, Booth J-P and Rousseau A 2013a Direct observation of ozone formation on SiO_2 surfaces in O_2 discharges *J. Phys. D: Appl. Phys.* **46** 032001

Marinov D, Guerra V, Guaitella O, Booth J-P and Rousseau A 2013b Ozone kinetics in low-pressure discharges: vibrationally excited ozone and molecule formation on surfaces *Plasma Sources Sci. Technol.* **22** 055018

Marinov D, Teixeira C and Guerra V 2017 Deterministic and Monte Carlo methods for simulation of plasma-surface interactions *Plasma Process. Polym.* **14** 1600175

Marschall J and MacLean M 2011 Finite-rate surface chemistry model, I: formulation and reaction system examples *AIAA Thermophysics Conf.* vol **42** p 3783

Meyer M, Foster J and Kushner M J 2023 A surface mechanism for O_3 production with N_2 addition in dielectric barrier discharges *Plasma Sources Sci. Technol.* **32** 085001

Morgan J E and Schiff H I 1964 Diffusion coefficients of O and N atoms in inert gases *Can. J. Chem.* **42** 2300–6

Morillo-Candás A S 2019 Investigation of fundamental mechanisms of CO_2 plasmas *PhD Thesis* École Polytechnique France

Mozetic M and Cvelbar U 2007 Heterogeneous recombination of O atoms on metal surfaces *Int. J. Nanosci.* **6** 121–4

Mozetic M, Vesel A, Stoica S D, Vizireanu S, Dinescu G and Zaplotnik R 2015 Oxygen atom loss coefficient of carbon nanowalls *Appl. Surf. Sci.* **333** 207–2013

Murphy A B and Park H 2017 Modeling of thermal plasma processes: the importance of two-way plasma-surface interactions *Plasma Process. Polym.* **14** 1600177

Nave S, Tiwari A K and Jackson B 2014 Dissociative chemisorption of methane on Ni and Pt surfaces: mode-specific chemistry and the effects of lattice motion *J. Phys. Chem.* A **118** 9615–31

Neyts E C and Brault P 2017 Molecular dynamics simulations for plasma-surface interactions *Plasma Process. Polym.* **14** 1600145

Oehrlein G S 1997 Surface processes in low pressure plasmas *Surf. Sci.* **386** 222–30

Pagnon D, Amorim J, Nahorny J, Touzeau M and Vialle M 1995 On the use of actinometry to measure the dissociation in O_2 DC glow discharges: determination of the wall recombination probability *J. Phys. D: Appl. Phys.* **28** 1856

Pandiyan A, Kyriakou V, Neagu D, Welzel S, Goede A, van de Sanden M C M and Tsampas M N 2022 CO_2 conversion via coupled plasma-electrolysis process *J. CO_2 Util.* **57** 101904

Paul D, Mozetic M, Zaplotnik R, Primc G, Donlagic D and Vesel A 2023 A review of recombination coefficients of neutral oxygen atoms for various materials *Materials* **16** 1774

Pfnür H, Feulner P, Engelhardt H A and Menzel D 1978 An example of “fast” desorption: anomalously high pre-exponentials for CO desorption from Ru (001) *Chem. Phys. Lett.* **59** 481

Rakhimova T V, Braginsky O V, Kovalev A S, Lopaev D V, Mankelevich Y A, Malykhin E M, Rakhimov A T, Vasilieva A N, Zyryanov S M and Baklanov M R 2009 Recombination of O and H atoms on the surface of nanoporous dielectrics *IEEE Trans. Plasma Sci.* **37** 1697–704

Rohnke M, Janeka J, Kilner J A and Chater R J 2004 Surface oxygen exchange between yttria-stabilised zirconia and a low-temperature oxygen rf-plasma *Solid State Ion.* **166** 89–102

Rutigliano M and Cacciatore M 2016 Recombination of oxygen atoms on silica surface: new and more accurate results *J. Thermophys. Heat Transfer* **30** 1–4

Seward W A and Jumper E J 1991 Model for oxygen recombination on silicon-dioxide surfaces *J. Thermophys.* **5** 284–91

Sholl D D 1997 Adsorption kinetics of chemisorption by surface abstraction and dissociative adsorption *J. Chem. Phys.* **106** 289–300

Silveira J N M 2023 Plasma-surface interactions in plasmas for CO_2 conversion *MSc Thesis* Instituto Superior Técnico - Universidade de Lisboa Portugal (unpublished)

Tait S L, Dohnálek Z, Campbell C T and Kay B D 2006 n-alkanes on Pt(111) and on C(0001)/Pt(111): chain length dependence of kinetic desorption parameters *J. Chem. Phys.* **125** 234308

Vanraes P, Venugopalan S P and Bogaerts A 2021 Multiscale modeling of plasma-surface interaction-general picture and a case study of Si and SiO_2 etching by fluorocarbon-based plasmas *Appl. Phys. Rev.* **8** 041305

Viegas P, Dias T C, Fromentin C, Chukalovsky A, Mankelevich Y, Proshina O, Rakhimova T, Guerra V and Voloshin D 2023 Comparison between 1D radial and 0D global models for low-pressure oxygen DC glow discharges *Plasma Sources Sci. Technol.* **32** 024002

Western C M, Booth J-P, Chatterjee A and de Oliveira N 2020 Rydberg spectra of singlet metastable states of O_2 *Mol. Phys.* **119** 1–2